

LIGHT PROPAGATION IN INHOMOGENEOUS UNIVERSES

II. COSMOLOGICAL PARAMETER SURVEY

PREMANA PREMADI^{1,2}, HUGO MARTEL³, RICHARD MATZNER^{4,5}, & TOSHIFUMI FUTAMASE²

¹ Department of Astronomy & Bosscha Observatory, Bandung Institute of Technology, Indonesia

² Astronomical Institute, Tohoku University, Sendai, Japan

³ Department of Astronomy, University of Texas, Austin, TX 78712

⁴ Center for Relativity, University of Texas, Austin, TX 78712

⁵ Department of Physics, University of Texas, Austin, TX 78712

ABSTRACT

Using a multiple-lens plane algorithm, we study light propagation in inhomogeneous universes, for 43 different *COBE*-normalized Cold Dark Matter models, with various values of the density parameter Ω_0 , cosmological constant λ_0 , Hubble constant H_0 , and rms density fluctuation σ_8 . This is the largest cosmological parameter survey ever done in this field. We performed a total of 3,798 experiments, each experiment consisting of propagating a square beam of angular size $21.9'' \times 21.9''$ composed of 116,281 light rays from the observer up to redshift $z = 3$. These experiments provide statistics of the magnification, shear, and multiple imaging of distant sources. The results of these experiments can be compared with observations, and eventually help constraining the possible values of the cosmological parameters. Additionally, they provide insight into the gravitational lensing process and its complex relationship with the various cosmological parameters.

Our main results are the following: (1) The magnification distribution depends mostly upon λ_0 and σ_8 . As σ_8 increases, the low-tail of the magnification distribution shifts toward lower magnifications, while the high-tail is hardly affected. The magnification distribution also becomes wider as λ_0 increases. This effect is particularly large for models with $\lambda_0 = 0.8$. (2) The magnification probability P_m is almost independent of σ_8 , for any combination of Ω_0 , λ_0 , H_0 , indicating that P_m does not depend strongly on the amount of large-scale structure. (3) The shear distribution, like the magnification distribution, depends mostly upon λ_0 and σ_8 . The shear distribution becomes wider with increasing σ_8 and increasing λ_0 . The similarities between the properties of the magnification and shear distributions suggests that both phenomena are caused by weak lensing. (4) About 0.3% of sources have multiple images. The double-image probability P_2 increases strongly with λ_0 and is independent of Ω_0 , H_0 , and σ_8 . (5) The distribution of image separations depends strongly upon λ_0 , and is independent of σ_8 . Summarizing these results, we find that (1) The properties of gravitational lensing, both weak and strong, depend much more strongly upon λ_0 than any other cosmological parameter, (2) magnification and shear are examples of weak lensing caused primarily by the distribution of background matter, with negligible contribution from galaxies, while multiple images and rings are examples of strong lensing, caused by direct interaction with galaxies, with negligible contribution from the background matter. Observations of weak lensing can be used to determine the cosmological constant and the density structure of the universe, while observations of strong lensing can be used to determine the cosmological constant and the internal structure of galaxies and clusters. Gravitational lensing depends much more weakly upon Ω_0 and H_0 than σ_8 and λ_0 , making a determination of these parameters from observations more difficult.

Accepted for publication in *The Astrophysical Journal Supplement* (June 2001)

1. INTRODUCTION

1.1. Importance of Gravitational Lensing in Cosmology

The evolution of a homogeneous, isotropic, expanding universe comprised of nonrelativistic matter can be described in terms of three parameters: the Hubble constant H_0 , the density parameter Ω_0 , and the cosmological constant λ_0 .⁶ Any combination of these three parameters corresponds to one particular cosmological model. The large-scale structure of the universe, galaxies, clusters, superclusters, and voids, represents the deviations from this overall homogeneity and isotropy. The most conservative assumption is that these structures originate from primordial fluctuations that grow with time as a result of gravitational instability. The fluctuations originate from a Gaussian random process, and are characterized entirely by a density fluctuation power spectrum. Determining the value of the cosmological parameters, and the correct model of large-scale structure formation, is the most important challenge of observational and physical cosmology.

Observing the present, nearby universe can only provide partial information about the value of the cosmological parameters, and the power spectrum of density fluctuations (see, e.g. Martel 1995). To unambiguously determine the correct cosmological model, it is crucial to observe the universe at high redshift (i.e. at large distances), to study its *past* structure and evolution, as well as its *global* geometry. Of all known redshift-dependent observational tests, gravitational lensing of distant sources is certainly the most powerful and most promising one.

Because sources must be located at cosmological distance for lensing effects to be important,⁷ most early work on gravitational lensing has focused on QSO's, being the farthest objects in the universe that were sufficiently luminous to be observable. However recent developments in instrumentation enable us to consider other sources at cosmological distances besides QSO's. The *Hubble Space Telescope* has deepened our field of view tremendously. The *Hubble Deep Field* (Williams et al. 1996) and *Southern Hubble Deep Field* (Williams et al. 1998) are the deepest sets of exposures even taken. Supernovae at redshifts $z = 0.95$ and $z = 1.32$ have been observed in these fields (Gilliland, Nugent, & Phillips 1999). These are the farthest supernovae ever seen, and as new instruments become available, it will be possible to observe supernovae at even larger redshifts, possibly up to $z = 20$ (Marri & Ferrara 1998).

High- z Type Ia supernovae have the potential to be much more useful than QSO's for gravitational lens studies. Unlike QSO's, Type Ia SNe are *nearly standard candles* (if we exclude the low-luminosity ones, which have limited cosmological use anyway). Although there are some variations in luminosity among Type Ia SNe, these variations are well-understood, and luminosities can be corrected (see the review by Filippenko & Riess 1998, and references therein). Having standard candles at cosmological distances has major implications for gravitational lensing studies. When a distant source is lensed by the intervening large-scale structure of the universe, it is usually magnified or demagnified, without multiple imaging. Only a small fraction of magnified sources are lensed sufficiently strongly to have multiple images, as we will show in this paper. Without multiple imaging (and without the resolution necessary to resolve the actual shape of the image), a magnified source may be mistaken for a source with a different luminosity, *unless the source is a standard candle*. If it is a standard candle, we can estimate its brightness from its known luminosity and estimated distance (based on redshift measurements). If the estimated brightness does not match the observed one, then the source is magnified, the magnification factor μ is given by the ratio of brightnesses, and the combination of the factor μ and the redshift z of the source yields information on the nature of the structures responsible for the lensing.

In recent years, gravitational lenses have been used to estimate or put limits on the values of the cosmological parameters. These studies have focused on the cosmological constant λ_0 (Fukugita, Futamase, & Kasai 1990; Turner 1990; Kochanek 1992, 1996a, 1996b; Krauss & White 1992; Maoz & Rix 1993; Bloomfield Torres & Waga 1996; Im, Griffiths, & Ratnatunga 1997; Chiba & Yoshii 1997, 1999), the density parameter Ω_0 (Yoshida & Omote 1992; Martínez-González, Sanz, & Cayón 1997), the (Ω_0, λ_0) plane (Asada 1997; Park & Gott 1997; Falco, Kochanek, & Muñoz 1998), the deceleration parameter q_0 (Wambsganss et al. 1997), the difference $\Omega_0 - \lambda_0$ (Cooray, Quashnock, & Miller 1999), or the Hubble constant H_0 (Watanabe,

⁶ Additional parameters must be included if the universe contains additional components such as radiation or quintessence.

⁷ We are not considering here the possibility of microlensing by nearby massive objects (like MACHO's).

Sasaki, & Tomita 1992; Falco et al. 1997; Keeton & Kochanek 1997; Kundić et al. 1997). All these studies were focussed on one or two particular cosmological parameters. In any such study, some assumption must be made about the value of the cosmological parameters that are *not* being determined. For instance, studies focusing on the cosmological constant all assume a flat universe ($\Omega_0 + \lambda_0 = 1$), while the studies focusing on the density parameter all assume a vanishing cosmological constant ($\lambda_0 = 0$). These assumptions are motivated more by theory than observations. The flatness of the universe is a requirement of the standard inflationary scenario (Guth 1981; Linde 1982; Albrecht & Steinhardt 1982), while a vanishing cosmological constant is the only known way to solve the cosmological constant problem (see, e.g. Weinberg 1989). As we shall see, several of these assumptions must be reconsidered in the light of recent observations.

1.2. The Need for a Full Cosmological Parameter Survey

During the 1980's, there was a strong theoretical prejudice in favor of the Einstein-de Sitter model ($\Omega_0 = 1, \lambda_0 = 0$). This model was particularly appealing because it satisfied the flatness requirement of the standard inflationary scenario, did not require a cosmological constant, and had fewer free parameters than any other model. Numerical simulations of large-scale structure formation (Davis et al. 1985; White et al. 1987) showed that an Einstein-de Sitter model in which the bulk of the matter is in form of Cold Dark Matter (CDM) could satisfy all the observational constraints known at the time. The theoretical prejudice for the Einstein-de Sitter model, supported by the numerical simulations of large-scale structure formation, led to the quasi-universal acceptance of the *Standard Cold Dark Matter Model* as the model of choice during the late 1980's. The only real difficulty that this model faced was the so-called age problem. In the standard CDM model (or any Einstein-de Sitter model), $H_0 t_0 = 2/3$. Independent measurements of the Hubble constant H_0 and the age of the universe t_0 showed that this constraint could be satisfied only marginally, as one needed to select the smallest possible values for both H_0 and t_0 . In particular, the value of H_0 had to be very near $50 \text{ km s}^{-1} \text{ Mpc}^{-1}$. Still, this difficulty was not regarded as serious enough to discard the standard CDM model.

Since then, there has been a tremendous increase in the number and quality of cosmological observations. These observations fall into three categories: low redshift observations (age of the universe, Hubble constant, deuterium abundance, baryon fraction in clusters, abundance of clusters, shape of the cluster mass function, large-scale velocity field), intermediate-redshift observations (Type Ia supernovae, gravitational lensing, cluster evolution, Ly α clouds), and high-redshift observations (cosmic microwave background). For details, we refer the reader to the recent reviews by Steigman, Hata, & Felten (1999), Martel & Matzner (2000), Ross & Harun-or-Rashid (2000), and Wang et al. (2000). These new observations impose numerous constraints on the cosmological parameters and the possible models of large-scale structure formation, and invariably argue against the standard CDM model. While the existence of cold dark matter is not ruled out, and indeed remains the best approach to explain galaxy and large-scale structure formation, the values of the cosmological parameters in the standard CDM model are essentially ruled out, as nearly all observations now support a universe with $\Omega_0 < 1$.

This forces us to consider alternatives to the standard CDM model. A low-density CDM model with $\Omega_0 < 1$, known as "Open CDM" or O Λ CDM is in much better agreement with most observations, but does not satisfy the flatness requirement of inflation. However, the possibility of "open inflation," or inflation without the flatness requirement, has been suggested by several authors (Ratra & Peebles 1994; Bucher, Goldhaber, & Turok 1995; Yamamoto, Sasaki, & Tanaka 1995; Linde 1995; Linde & Mezhlumian 1995), and is supported by some recent observations (Filippenko & Riess 1998). But if we stick to the flatness requirement of the standard inflationary scenario, then we must include in the model an additional smooth component to account for the difference between Ω_0 and 1. Numerous candidates have been proposed (see, e.g. Fry 1985; Charlton & Turner 1987), but the most promising ones at present are the cosmological constant and the quintessence (see Turner 1999 for a recent review). The corresponding models, Λ CDM and QCDM, have $\Omega_0 + \Omega_S = 1$, where Ω_S is the effective density parameter associated with the smooth component.

In the standard CDM model, the primordial power spectrum of density fluctuations is assumed to have the Harrison-Zel'dovich form $P(k) \propto k$ at large scales. This power spectrum can be modified by introducing a "tilt." In this Tilted CDM, or TCDM model, the primordial power spectrum $P(k)$ varies as $P(k) \propto k^n$ at large scales, where the primordial exponent n can differ from unity. With an exponent n of order $0.8 - 0.9$,

it is possible to reconcile the constraints imposed by the CMB anisotropies and the present abundance of clusters with a density parameter $\Omega_0 < 1$, without the addition of a cosmological constant or quintessence.

To discriminate between these various models, we must determine the values of the cosmological parameters. The standard CDM model had no free parameter: the density parameter was unity, and the Hubble constant was severely constrained by the age problem. These alternative CDM models have many free parameters: the density parameter Ω_0 , the cosmological constant λ_0 (or the effective density parameter associated with quintessence), the Hubble constant H_0 , and the tilt n of the primordial power spectrum. Gravitational lensing of distant sources provides a powerful tool for studying the structure and evolution of the large-scale structure in the universe, and eventually constrain the value of these cosmological parameters. However, all the previous studies listed in §1.1 focused on only one or two parameters, while assuming some particular values for the other parameters. If the correct cosmological model has several free parameters, it is clearly impossible to determine the value of these parameters separately. This would be like looking for a fugitive in a city, but limiting the search to one street and one avenue only. A full survey of the cosmological parameter space is required in order to determine or limit the values of all cosmological parameters *simultaneously*. In this paper, we present the first study of light propagation in inhomogeneous universe that surveys the full 4-parameter phase-space formed by Ω_0 , λ_0 , H_0 , and n .

1.3. Objectives

There are two distinct objectives to this study. The first one is to determine the properties of lensed sources, such as their magnification distributions, shear distributions, image separations, and so on; properties which depend upon the value of the cosmological parameters. By directly comparing the predictions of the simulations with current and future observations of gravitational lens systems, we hope to eventually constrain the values of the cosmological parameters, and the possible scenarios of large-scale structures and galaxy formation.

The second objective is more theoretical in nature. By studying the properties of gravitational lenses, and how these properties depend upon the values of the cosmological parameters, individually or in combination, we can gain insight into the phenomenon of light propagation in inhomogeneous universe and its relationship to the underlying cosmological model. This objective is more ambitious than the first one: instead of merely determining which particular model reproduces observations better, we wish to understand the *reason* which favors this particular model. Achieving this second objective requires that we extend the parameter survey to regions of the parameter space that are not particularly favored by observations. This forced us to consider a record number of cosmological models in this study, and even with 43 models, our covering of the 4-dimensional parameter space is patchy at best.

The various effects of gravitational lensing can be divided into two broad categories: weak lensing and strong lensing.⁸ Weak lensing is caused by the smooth distribution of matter, with moderate density contrast, located between the source and the observer. The magnification or demagnification of sources, or the shear — circular sources having elliptical images — are examples of weak lensing. Weak lensing provides an unbiased information about the matter distribution in the universe, as well as the underlying geometry, that can be used to constrain cosmological models (Bacon, Refregier, & Ellis 2000; van Waerbeke et al. 2000; Munshi & Coles 2000; Jain, Seljak, & White 2000). Strong lensing involves direct interaction between the beam and large mass concentrations such as galaxies and cluster of galaxies. Strong lensing causes spectacular events such as multiple images, giant arcs, and Einstein rings, providing mostly information about the density structure of the lens itself (Schneider, Ehlers, & Falco 1992, hereafter SEF, chapter 8), though some properties of strong lensing can be used to determine the cosmological parameters as well. For instance, the time delay between multiple images of a single source can be used to determine the Hubble constant. Most previous studies have focused either on weak lensing or strong lensing. One important goal of our work is to study the properties of weak and strong lensing simultaneously. To achieve this, we must use an algorithm that can resolve cosmic structures over a very large dynamical range in length, from the size of cluster and superclusters down to the central cores of galaxies. This led to the development of a new version of the multiple lens-plane algorithm, based on earlier work by Jaroszyński (see §2 below).

⁸ Microlensing would be a third category, which we are not considering in this paper.

Because of the nature of these objectives, this project involved an amount of effort that is quite substantial compared with similar studies that have been performed and published by various authors in recent years. We are studying a record number of cosmological models, 43. We have performed a total of 3,798 ray-tracing experiments.⁹ In order to study the properties of weak and strong lensing simultaneously, we used beams composed of a very large number of light rays, 116,281. Overall, we have simulated the propagation in inhomogeneous universes of 441,635,238 light rays. We have generated the images of 3,137,675 extended sources located at redshift $z = 3$. For each and every one of these images, we have computed the magnification and aspect ratio, and whenever we encountered special kinds of images, such as multiple images and rings, we studied their properties, such as image separations, brightness ratios, and hole diameters. The calculations started on a Cray J90 supercomputer, and later moved to a more powerful Cray SV1 supercomputer. The N -body simulations used to generate the large-scale structure for the various cosmological models (3 simulations for each of the 43 models, for a total of 129 P³M simulations with one quarter million particles each) took about 2000 CPU hours, while the ray-tracing experiments took about 600 CPU hours.

The remainder of this paper is organized as follows: in §2, we describe the numerical algorithm used for the simulations. In §3, we describe the cosmological models included in the study, the ray-tracing experiments, and the technique used for analyzing the results. In §4, we review the various elements that affect gravitational lensing. Results are presented in §5, including the magnification distributions (§5.1), the magnification probability (§5.2), the shear distributions (§5.4), the multiplicity of images (§5.5), the distribution of image separations (§5.6), and the properties of Einstein Rings (§5.7). In §6, we discuss the various approximations implied by the algorithm and their possible effects on the results. Summary and conclusions are presented in §7.

2. THE MULTIPLE LENS-PLANE ALGORITHM

Our numerical algorithm was described in detail by Premadi, Martel, & Matzner (1998, hereafter Paper I), and convergence tests of the algorithm were presented by Martel, Premadi, & Matzner (2000). In this section, we give a brief summary of the method, and describe some minor refinements that have been introduced into the algorithm since the publication of Paper I.

A light ray traveling from a distant source to the observer is affected continuously by the distribution of matter it encounters along its trajectory. The multiple lens-plane algorithm (SEF, and references therein) consists of approximating this continuous effect by a finite number of instantaneous deflections, caused by the matter distribution encountered at various locations along the trajectory of the ray. To implement this method, we divide the space between the source and the observer into redshift intervals, and project the matter inside each interval onto a plane normal to the line of sight, called a lens plane. Every lens plane deflects the light rays that go through it, and the deflection angles can be computed using geometrical optics. We can then follow the evolution of a light beam propagating through the universe, by adding successively the contributions of each lens plane to the deflection and deformation of the beam. During the past decade, this method has been one of the main tools for studying the properties of gravitational lenses located at cosmological distances (Blandford & Nayaran 1986; Blandford & Kochanek 1987; Schneider & Weiss 1988a, b; Jaroszyński et al. 1990; Jaroszyński 1991, 1992; Babul & Lee 1991; Bartelmann & Schneider 1991; Wambsganss, Cen, & Ostriker 1996; Bartelmann et al. 1998; Couchman, Barber, & Thomas 1999; van Waerbeke, Bernardeau, & Mellier 1999; Hamana, Martel, & Futamase 2000; Jain et al. 2000; see also Kochanek & Apostolakis 1988; Paczyński & Wambsganss 1989; for an interesting alternative, see Fluke, Webster, & Mortlock 1999).

What usually distinguishes a particular version of the multiple lens-plane algorithm from other versions is the method used for representing the surface density on the lens planes. The issue of length resolution is critical. The magnification of the images of distant sources depends essentially on the amount of matter located near the beam, along the line of sight. However, the deformation (or shear) of the images results primarily from the tidal influence of distant matter. Therefore, to accurately simulate the effect of both magnification and shear, we must reproduce the surface density of the lens planes over the largest possible dynamical range in length. Our algorithm achieves a very high length resolution by combining numerical

⁹ An additional 101 experiments were performed afterward, to answer some specific questions raised by an anonymous referee, concerning the angular size of the sources.

simulations of large-scale structure formation with a Monte-Carlo method for locating galaxies inside these structures. This approach was pioneered by Jaroszyński (1991, 1992).

2.1. Large-Scale Structure Formation

We use a Particle-Particle/Particle-Mesh (P³M) code (Hockney & Eastwood 1981) to simulate the formation and evolution of large-scale structure in the universe. The algorithm produces snapshots of the large-scale structure at various redshifts. If we interpret these redshifts in terms of distances from the observer, we can treat each snapshot as representing a different region of the universe, and by combining them, we can build a chain of cubic boxes representing the large-scale structure over distances of Gigaparsecs, from the observer to distant sources. We can then project the matter distribution inside each box onto one lens plane. Since different boxes represent different regions of the universe, the large-scale structure inside neighboring boxes should be uncorrelated. This is clearly a problem if the boxes originate from one single simulation, since they would then represent the same large-scale structure at various evolutionary stages. To solve this problem, we perform three independent calculations for each cosmological model, by using three different sets of initial conditions. We then combine the results of these simulations, such that the first simulation provides boxes 1, 4, 7, . . . along the line of sight, the second simulation provides boxes 2, 5, 8, . . ., and the third simulation provides boxes 3, 6, 9, . . ., thus ensuring that two consecutive boxes never come from the same calculation. To reduce correlations even more, we make use of the periodic boundary conditions of the simulations, by giving to the matter distribution in each box a random shift.

For all P³M simulations, we use 64³ particles and a 128³ grid, inside a cubic box of comoving size $L_{\text{box}} = 128 \text{ Mpc}$. The comoving softening length of the algorithm is 300 kpc. The total mass of the system is $M_{\text{sys}} = 3H_0^2\Omega_0 L_{\text{box}}^3/8\pi G = 5.821 \times 10^{17}(\Omega_0 h^2)M_\odot$. The mass per particle is $m = M_{\text{sys}}/64^3 = 2.220 \times 10^{12}(\Omega_0 h^2)M_\odot$. We performed a total of 129 simulations (3 per model for 43 models).¹⁰

2.2. The Galaxies Distributions

The large-scale structure simulations described in §2.1 can be used to compute the effect of distant matter on the propagation of the beam. However, at distances less than a few megaparsecs, we cannot ignore the fact that matter has collapsed to form galactic-size objects which are much smaller than the resolution of the P³M algorithm.¹¹ We cannot extend the resolution of the P³M code down to galactic scales, because simulating the galaxy formation process would require additional physics besides gravity, such as hydrodynamical and radiative processes. Instead, we complement the P³M algorithm with an empirical Monte Carlo method for locating galaxies inside the computational volume, based on the underlying distribution of dark matter (Jaroszyński 1991, 1992; Paper I; Martel, Premadi, & Matzner 1998).

First, we need to determine the number of galaxies present in the computational volume. We assume that the present galaxy luminosities follow a Schechter luminosity function,

$$n(L)dL = \frac{n_*}{L_*} \left(\frac{L}{L_*} \right)^\alpha e^{-L/L_*} dL, \quad (1)$$

where $n(L)$ is the number density of galaxies per unit luminosity. We use the values $\alpha = -1.10$, $n_* = 0.0156 h^3 \text{ Mpc}^{-3}$, and $L_* = 1.3 \times 10^{10} h^{-2} L_\odot$, where h is the Hubble constant in units of $100 \text{ km s}^{-1} \text{ Mpc}^{-1}$ (Efstathiou, Ellis, & Peterson 1988). There is a fourth parameter, the luminosity L_{min} of the faintest galaxies, which must be introduced to prevent the total number of galaxies from diverging. The value of this parameter is not well-known. We assume a value of $L_{\text{min}} = 0.01L_*$

Equation (1) allows us to directly compute the present number density n_0 , and luminosity density j_0 ,

$$n_0 = n_* \int_{x_{\text{min}}}^{\infty} x^\alpha e^{-x} dx = n_* \Gamma(\alpha + 1, x_{\text{min}}), \quad (2)$$

$$j_0 = n_* L_* \int_{x_{\text{min}}}^{\infty} x^{\alpha+1} e^{-x} dx = n_* L_* \Gamma(\alpha + 2, x_{\text{min}}), \quad (3)$$

¹⁰ These simulations now constitute the core of the *Texas P³M Database* (Martel & Matzner 2000).

¹¹ The universe also contains virialized objects at larger scales, but these are properly simulated by the P³M algorithm.

where $x \equiv L/L_*$, $x_{\min} \equiv L_{\min}/L_*$, and Γ is the incomplete Gamma function. For $x_{\min} = 0.01$, equations (2) and (3) give $n_0 = 0.0808 h^3 \text{Mpc}^{-3}$ and $j_0 = 2.13 \times 10^8 h L_{\odot} \text{Mpc}^{-3}$. The total number of galaxies in the computational volume is given by

$$N_{\text{gal}} = n_0 L_{\text{box}}^3 = n_* L_{\text{box}}^3 \Gamma(\alpha + 1, x_{\min}). \quad (4)$$

For $L_{\text{box}} = 128 \text{Mpc}$, equation (4) gives $N_{\text{gal}} = 28200, 46500, 71500,$ and 104000 , respectively, for the values $h = 0.55, 0.65, 0.75,$ and 0.85 considered in this paper (see §3.1 below).

We use a Monte-Carlo rejection method for determining the location of the galaxies in the computational volume at present ($z = 0$). We divide the computational volume in cubic cells of size $(1 \text{Mpc})^3$, and locate a certain number of galaxies in each cell. That number is chosen from a Gaussian distribution with a standard deviation proportional to the total matter density in that cell, determined from the distribution of particles in the P³M simulation.¹² The proportionality constant is chosen in order to reproduce the number of galaxies N_{gal} given by equation (4). The actual location of each galaxy is chosen to be the center of the cell, plus a random offset of order of the cell size, also chosen from a Gaussian distribution. With our particular choice of cell size, this method naturally creates compact groups of galaxies, with separations comparable to the ones found in the Local Group, for instance. Once the position of each galaxy in the computational volume at present is known, we reconstruct the trajectories of galaxies, and determine their locations at any redshift, by following the trajectory of the P³M particle nearest to each galaxy (a similar method was used in Jaroszyński 1991, 1992).

Tests have shown that this method produces realistic galaxy distributions (Paper I). In particular, the observed 2-point correlation function of galaxies is well reproduced down to separations of order of the cell size, 1 Mpc.

Each galaxy is modeled by a truncated, non-singular isothermal sphere, whose parameters depend upon the galaxy luminosity and morphological type. We adopt the galaxy models described by Jaroszyński (1991, 1992). The projected surface density of each galaxy is given by

$$\sigma(r) = \begin{cases} \frac{v^2}{4G(r^2 + r_c^2)^{1/2}}, & r < r_{\max}; \\ 0, & r > r_{\max}; \end{cases} \quad (5)$$

where r is the projected distance from the center. The parameters r_c , r_{\max} , and v are the core radius, maximum radius, and rotation velocity, respectively, and are given by

$$r_c = r_{c0} \left(\frac{L}{L_*} \right), \quad (6)$$

$$r_{\max} = r_{\max 0} \left(\frac{L}{L_*} \right)^{1/2}, \quad (7)$$

$$v = v_0 \left(\frac{L}{L_*} \right)^{\gamma}, \quad (8)$$

where the parameters r_{c0} , $r_{\max 0}$, v_0 , and γ are given in Table 1 (Chiba & Futamase [1999], used a similar approach, with different values for the parameters). We use a Monte-Carlo method to generate for each galaxy a luminosity $L \geq L_{\min}$, with a probability $P(L)$ proportional to $n(L)$. We determine the morphological type of each galaxy by using the observed *morphology-density relation* (Dressler 1980; Postman & Geller 1984). Regions of the sky with high concentration of galaxies contain on average more early-type galaxies (ellipticals and S0's) and fewer late-type galaxies (spirals) than regions with lower concentration of galaxies. By combining this relation with a Monte-Carlo method, we can ascribe a morphological type to each galaxy. This can be quite important. Several authors (e.g. Krauss & White 1992; Kochanek 1996a) have found that the lensing effect of galaxies is much more important for ellipticals than for spirals, mostly because ellipticals

¹² The use of a Gaussian distribution is an improvement over the original algorithm presented in Paper I, because it allows for the presence of galaxies in low-density regions.

have a smaller core radius. Consequently, it is not sufficient to have a realistic distribution of galaxies: the distribution must be realistic *within each morphological type*, otherwise, some effects, such as strong double lensing by pairs of elliptical galaxies, would be underestimated.

TABLE 1: Galaxy Parameters

Type	r_0 ($h^{-1}\text{kpc}$)	$r_{\text{max}0}$ ($h^{-1}\text{kpc}$)	v_0 (km s^{-1})	γ
Elliptical	0.1	30	390	0.250
S0	0.1	30	357	0.250
Spiral	1.0	30	190	0.381

By combining the distribution of background matter simulated by the P³M algorithm with the distribution and surface densities of galaxies, we are effectively describing the surface density of the lens planes over 8 orders of magnitude in length, from the size of the largest superclusters and voids, ~ 100 Mpc, down to the core radii of the smallest galaxies, ~ 1 pc. The combination of fully nonlinear large-scale structure formation, galaxy distributions that reproduce the observed 2-point correlation function, morphological type distributions that reproduce the observed morphology-density relation, and galaxy surface density profiles, gives to the matter distribution in our algorithm a level of realism that was not present in any of the previous studies.

Figure 1 illustrates the dynamical range that can be achieved with this method. The top left panel shows the large scale structure of the universe as simulated by the P³M code, for a box of 128 Megaparsecs in size. The dots are the particles used by the P³M algorithm, and are therefore mass-tracers. This panel shows a complex network of clusters, filaments, and voids. We enlarge a region of size 10 Mpc and display it on the top right panel. At that scale, we see several irregular clusters. The dots still represent the particles used in the P³M code. We enlarge the central cluster, and display it on the middle right panel. In addition to the P³M particles, we also plot the galaxies (large dots), whose locations were determined by the Monte-Carlo part of the algorithm. We isolate a group of 5 galaxies in this cluster, and plot them at a smaller scale on the middle left panel. This group, which is about 3 times smaller than our own “local group,” is composed of 3 spiral galaxies, one S0 galaxy, and one elliptical galaxy. We enlarge the central galaxy, and display it on the bottom left panel. The large circle represents the edge of the dark-matter halo (radius $r = r_{\text{max}}$). The central dot represents the galactic core. We enlarge this core, which has a radius $r = r_c$, and display it in the bottom right panel. There are 7 orders of magnitudes in length between the diameter of this core and the size of the largest structures shown on the top left panel, and some galaxies in the simulation have a core which is an order of magnitude smaller than the one represented here.

3. THE COSMOLOGICAL PARAMETER SURVEY

3.1. The Cosmological Models

All models considered in this paper are Tilted Cold Dark Matter models (TCDM), normalized according to the results of the *COBE* DMR experiment. The density fluctuation power spectrum for these models is described in great detail in Bunn & White (1997). The power spectrum at the initial redshift z_i is given by

$$P(k, z_i) = 2\pi^2 \left(\frac{c}{H_0} \right)^{3+n} \delta_H^2 \mathcal{L}^{-2}(z_i, 0) k^n T_{\text{CDM}}^2(k). \quad (9)$$

where c is the speed of light, H_0 is the Hubble constant, and $\mathcal{L}(z_i, 0)$ is the linear growth factor between the initial redshift z_i and the present, and T_{CDM} is the transfer function, given by

$$T_{\text{CDM}}(q) = \frac{\ln(1 + 2.34q)}{2.34q} [1 + 3.89q + (16.1q)^2 + (5.46q)^3 + (6.71q)^4]^{-1/4} \quad (10)$$

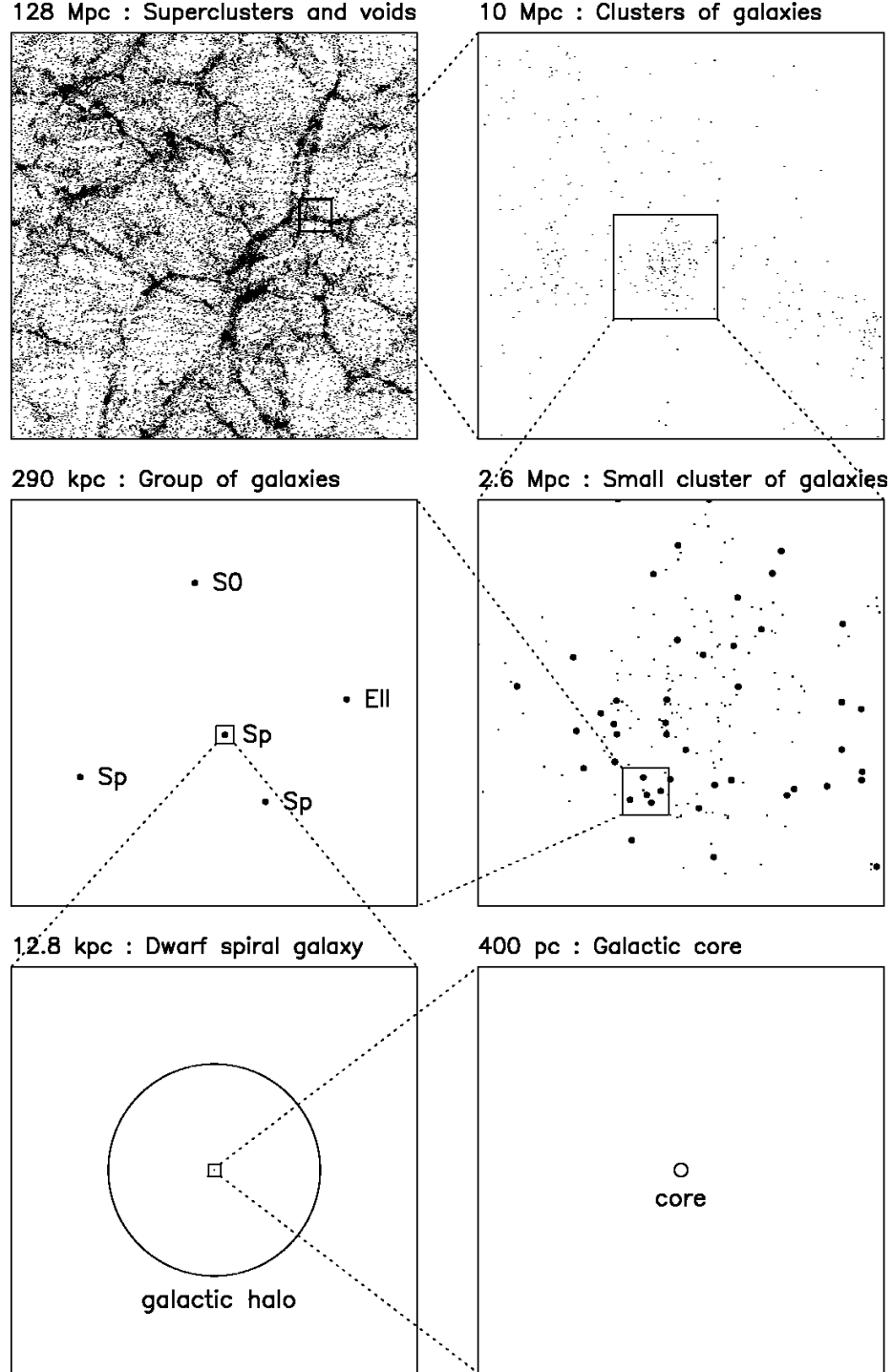


Figure 1: Series of zooms illustrating the dynamical range of the algorithm. Top left panel: Distribution of background matter projected on a lens plane at $z = 0$; Top right panel: Enlargement of a dense region, showing several clusters of galaxies; Middle right panel: A particular cluster of galaxies. Small dots represent P^3M , dark matter particles. Large dots represent actual galaxies; Middle left panel: A small group of galaxies inside the cluster, composed of 3 spirals, one S0, and one elliptical. Bottom left panel: A particular spiral galaxy, with a halo radius r_{\max} given by equation (7); Bottom right panel: The core of the spiral galaxy, with a radius r_c given by equation (6).

(Bardeen et al. 1986), with q defined by

$$q = \left(\frac{k}{\text{Mpc}^{-1}} \right) \alpha^{-1/2} (\Omega_0 h^2)^{-1} \Theta_{2.7}^2, \quad (11)$$

$$\alpha = a_1^{-\Omega_{\text{B}0}/\Omega_0} a_2^{-(\Omega_{\text{B}0}/\Omega_0)^3}, \quad (12)$$

$$a_1 = (46.9 \Omega_0 h^2)^{0.670} [1 + (32.1 \Omega_0 h^2)^{-0.532}], \quad (13)$$

$$a_2 = (12.0 \Omega_0 h^2)^{0.424} [1 + (45.0 \Omega_0 h^2)^{-0.582}], \quad (14)$$

(Hu & Sugiyama 1996, eqs. [D-28] and [E-12]), where $\Omega_{\text{B}0}$ is the density parameter of the baryonic matter, and $\Theta_{2.7}$ is the temperature of the cosmic microwave background in units of 2.7K. The density fluctuation δ_H at horizon scale is given by

$$\delta_H = \begin{cases} 1.95 \times 10^{-5} \Omega_0^{-0.35-0.19 \ln \Omega_0 - 0.17 \tilde{n}} e^{-\tilde{n} - 0.14 \tilde{n}^2}, & \lambda_0 = 0; \\ 1.94 \times 10^{-5} \Omega_0^{-0.785-0.05 \ln \Omega_0} e^{-0.95 \tilde{n} - 0.169 \tilde{n}^2}, & \lambda_0 = 1 - \Omega_0; \end{cases} \quad (15)$$

where $\tilde{n} \equiv n - 1$.

This power spectrum is characterized by 6 independent parameters: Ω_0 , $\Omega_{\text{B}0}$, λ_0 , H_0 , T_{CMB} , and n . The normalization of the power spectrum is often described in terms of the rms density fluctuation σ_8 at a scale of $8h^{-1}\text{Mpc}$, defined by

$$\sigma_8^2 = \frac{1}{2\pi^2} \int_0^\infty P(k) W^2(k\ell) k^2 dk, \quad (16)$$

where $\ell = 8h^{-1}\text{Mpc}$, and W is the window function, given by

$$W(x) = \frac{3}{x^3} (\sin x - x \cos x). \quad (17)$$

The value of σ_8 is a function of the 6 aforementioned parameters. We invert this relation, treating σ_8 as an independent parameter, and the tilt n as a dependent one. We also set $T_{\text{CMB}} = 2.7\text{K}$ and $\Omega_{\text{B}0} = 0.015h^{-2}$ for all models, thus reducing the dimensionality of the parameter-space from 6 to 4.¹³ The independent parameters in this parameter space are therefore Ω_0 , λ_0 , H_0 , and σ_8 .

We survey this parameter space by considering 43 different cosmological models. This constitutes the largest parameter survey ever done in this field. The values of the parameters are listed in the first 4 columns of Table 2, while the values of the dependent parameter n are listed in the fifth column. The values of σ_8 were chosen by imposing that n remains in the range [0.7, 1.3].

3.2. The Ray-Tracing Experiments

For each model, we performed numerous ray-tracing experiments. The number of experiments for each model is listed in the sixth column of Table 2. In each experiment, we compute the propagation of a beam consisting of $341^2 = 116,281$ light rays forming a square lattice on the image plane. The size of the beam is $21.9'' \times 21.9''$, and the separation between rays is $21.9''/341 = 0.064''$. This is significantly smaller than the typical size of an emitting region. A source of angular diameter $1''$ will contain 190 rays (more if the source is magnified), enough to resolve details such as multiple images. We locate the source plane at a redshift $z_S = 3$, which is a reasonable choice. The effect of lensing would be more important for sources at larger redshifts, but these sources would be more difficult to observe. By choosing $z_S = 3$, we hope to obtain results that can be compared with current observations. For a list of the source redshifts used in similar calculations, see Table 3 in Martel et al. (2000). The redshift intervals between the lens planes were chosen as in Paper I, §3.2.2.

¹³ Recent results support $\Omega_{\text{B}0} = 0.0193h^{-2}$ (Burles & Tytler 1998), a value slightly larger than the one we assumed. The difference is too small to affect the power spectrum in any significant way, for any of the models considered.

TABLE 2: Parameters of the Models

Ω_0	λ_0	H_0	σ_8	n	N_{exp}
0.2	0.0	55	0.3	1.2187	99
0.2	0.0	65	0.3	1.0966	92
0.2	0.0	65	0.5	1.3188	104
0.2	0.0	75	0.3	0.9993	47
0.2	0.0	75	0.4	1.1228	199
0.2	0.0	75	0.5	1.2190	70
0.2	0.0	75	0.6	1.2979	51
0.2	0.0	75	0.7	1.3648	199
0.2	0.0	85	0.3	0.9191	101
0.2	0.8	55	0.8	1.2057	99
0.2	0.8	65	0.6	0.9326	70
0.2	0.8	65	0.7	1.0062	51
0.2	0.8	65	0.8	1.0702	108
0.2	0.8	65	0.9	1.1269	50
0.2	0.8	65	1.0	1.1568	67
0.2	0.8	75	0.6	0.8273	51
0.2	0.8	75	0.8	0.9629	51
0.2	0.8	85	0.8	0.8749	45
0.5	0.0	65	0.8	0.9457	48
0.5	0.0	65	1.0	1.0439	77
0.5	0.0	75	0.8	0.8686	51
0.5	0.0	75	1.0	0.9656	50
0.5	0.5	65	0.8	0.7808	105
0.5	0.5	65	1.0	0.8807	62
0.5	0.5	75	0.8	0.7049	51
0.5	0.5	75	1.0	0.8024	51
0.7	0.0	65	0.9	0.8461	96
0.7	0.0	65	1.1	0.9346	60
0.7	0.0	75	0.9	0.7773	50
0.7	0.0	75	1.1	0.8648	50
0.7	0.3	65	0.9	0.7720	64
0.7	0.3	65	1.1	0.8601	77
0.7	0.3	75	0.9	0.7042	51
0.7	0.3	75	1.1	0.7912	46
1.0	0.0	55	1.0	0.8465	145
1.0	0.0	65	0.9	0.7234	184
1.0	0.0	65	1.0	0.7698	156
1.0	0.0	65	1.1	0.8120	175
1.0	0.0	65	1.2	0.8506	168
1.0	0.0	65	1.3	0.8861	176
1.0	0.0	75	1.0	0.7094	142
1.0	0.0	75	1.2	0.7893	58
1.0	0.0	85	1.0	0.6605	51

3.3. Analyzing the Distribution of Light Rays

To analyze the results of the experiments, we lay down on the source plane a square grid composed of $31 \times 31 = 961$ square cells. The location and size of the grid are adjusted such that, in the absence of lensing, the edges of the grid would correspond to the edges of the beam. Figure 2 shows the beam configuration and the grid on the source plane, for a typical experiment. In the absence of lensing, each cell would contain 121 rays. A source located in a cell containing more than 121 rays would be magnified, whereas a source located in a cell containing less than 121 rays would be demagnified. By counting the number of rays in each cell, we can then compute a magnification map. The magnification $\mu_{e,i}$ in cell i for experiment e is then given by

$$\mu_{e,i} = \frac{N_{e,i}}{\langle N \rangle}, \quad (18)$$

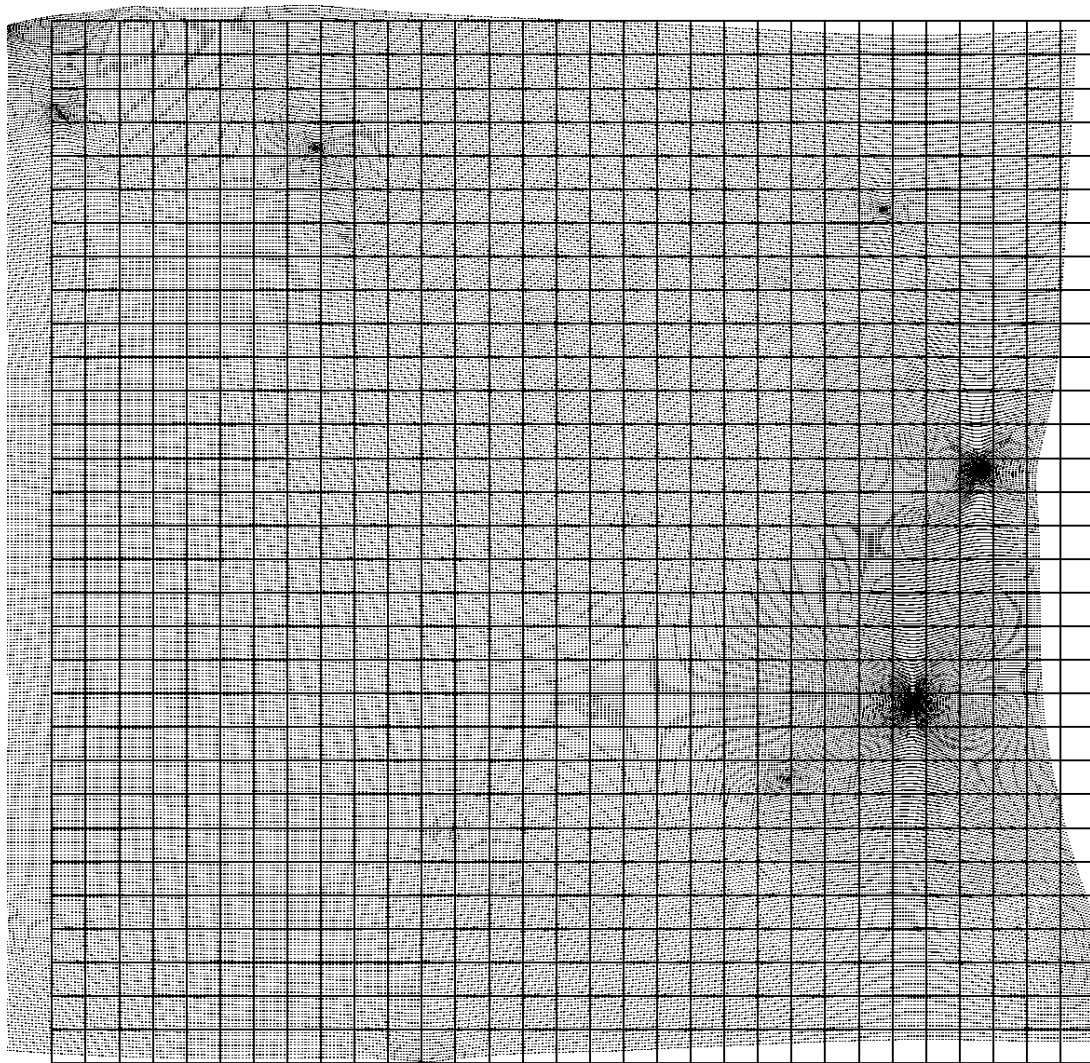


Figure 2: Configuration of the beam on the source plane, for a typical experiment. Each dot represents one light ray. The square grid that we lay down on the source plane is also indicated. In the absence of lensing, the beam would coincide with the grid, and each cell would contain 11×11 light rays.

where $N_{e,i}$ is the number of rays in cell i for experiment e , and $\langle N \rangle$ is the average number of rays per cell. Looking at Figure 2, we see many cells located along the edges of the grid that are empty or partially empty.

This is of course a numerical artifact caused by the finite size of the beam. These cells should be excluded from the analysis, otherwise they would artificially bias the magnification distributions toward low values. Our original approach was to exclude all cells located along the edges of the grid, using only the inner 29×29 cells instead of the full 31×31 . However, this proved insufficient in cases of large beam deformation, such as the case shown in Figure 2. For this reason, we exclude all cells that are along the edges of the grid, plus any cell that is adjacent to an empty cell, since that cell might be half-empty, or even completely empty. In Figure 3, we show an enlargement of the right edge of Figure 2. The cells located on the left of the thick line are included in the analysis, but the ones on the right are excluded: 6 of them are along the edge of the grid, and 3 others are adjacent to empty cells.

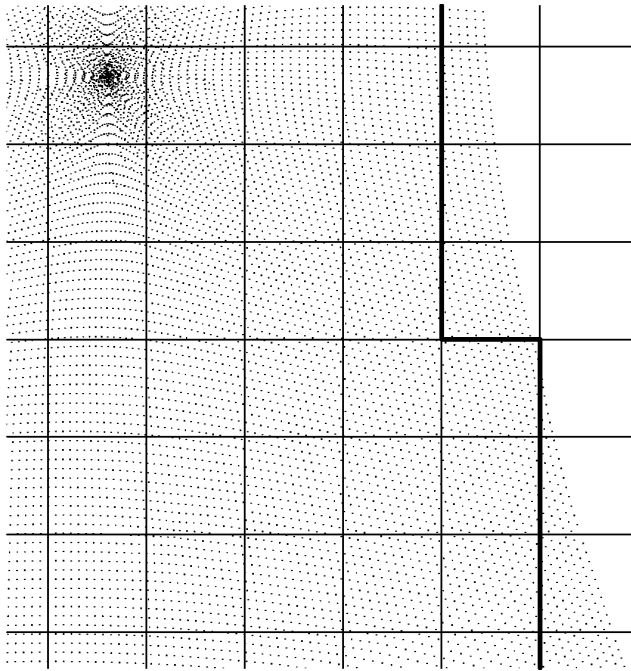


Figure 3: Enlargement of the right edge of Figure 2. The thick line separates cells that are included in the analysis (on the left) and cells that are excluded (on the right), either because they are along the edge of the grid or because they are adjacent to an empty cell.

The number of rays exceeds the number of cells by a factor of 121. There are two reasons for using such a large number of rays. First, if the number of rays were comparable to the number of cells, the magnification map would be very sensitive to the actual location of the grid. With an average of 121 rays per cell, the sensitivity to grid location is significantly reduced. Second, with a large number of rays per cell, we can study the properties of the images. Each cell on the source plane constitutes a potential location for a source. Assuming that a particular cell contains a source, we can identify the light rays contained in that cell and trace back these rays on the image plane. This enables us to study the properties of images, such as multiplicity, angular separations, brightness ratios, and shapes (simple images, arcs, rings, . . .). An obvious problem is that the cells are squares, while sources are expected to be circular. We solve this problem by superposing over each square cell a circular cell whose diameter is equal to the diagonal of the square cell, as shown in Figure 4. These circular cells have an angular diameter of $1''$, and in the absence of lensing, each one would contain $\langle N \rangle = 121(\pi/2) = 190$ rays.

4. THE ELEMENTS OF GRAVITATIONAL LENSING

Before we discuss the results of the experiments, we first review the various elements that enter into gravitational lensing, and the relationship between these elements and the cosmological parameters. This will facilitate the interpretation of the results presented in the following section.

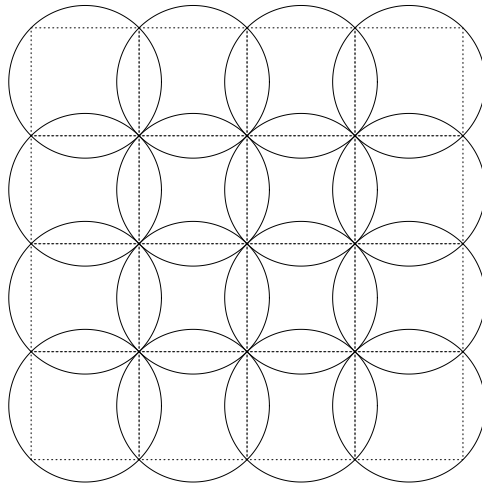


Figure 4: Dashed lines: portion of the square grid laid down on the source plane. Solid circles: Circular cells superposed on the square cells.

4.1. The Cosmological Distances

The angular displacement of rays caused by lensing depends critically on the angular diameter distances between the source and the observer, D_S , the source and the lens, D_{LS} , and the lens and the observer, D_L . In our simulations, there is a continuous distribution of matter between the source and the observer (approximated by a finite number of lens planes). In this context, the term “lens” refers to the fraction of that matter distribution that is primarily responsible for lensing. The amount of lensing depends on the product $D_L D_{LS}$, which is maximum for $D_L \simeq D_{LS}$. Hence, lensing is caused primarily by the matter located about half-way between the source and the observer. As we discussed in Paper I, this distance effect is competing with two other effects: First, the large-scale structure, which is responsible for lensing, grows with time, favoring lenses that are closer to the observer. Second, for a fixed number of galaxies, the number density of galaxies decreases with time as the universe expands, and therefore the beam is more likely to hit a galaxy at locations that are closer to the source. We found in Paper I that the distance effect dominates over the other effects, and therefore the matter located half-way between the source and the observer is responsible for most of the lensing. The only exception is the Einstein-de Sitter model, in which the large-scale structure keeps growing all the way to the present. The matter responsible for most of the lensing tends to be located somewhat closer to the observer than the half-way point. This effect is negligible for other models because the large-scale structure does not grow all the way to the present, but instead freezes-out at some redshift of order $z_{fr} \sim 1/\Omega_0$.

If the distance effect dominates, then the source redshift determines the “lens” redshift, and therefore only one distance, say D_S , is independent. This distance is given by

$$D_S = \frac{c}{H_0} f(\Omega_0, \lambda_0, 0, z_s), \quad (19)$$

where the function f is given by:

$$f(\Omega_0, 0, z_i, z_j) = \frac{2 \left[(2 - \Omega_0 + \Omega_0 z_j)(1 + \Omega_0 z_i)^{1/2} - (2 - \Omega_0 + \Omega_0 z_i)(1 + \Omega_0 z_j)^{1/2} \right]}{\Omega_0^2 (1 + z_i)(1 + z_j)^2}, \quad (20)$$

$$f(\Omega_0, 1 - \Omega_0, z_i, z_j) = \frac{1}{1 + z_j} \int_{z_i}^{z_j} dz \left[\Omega_0 (1 + z)^3 + (1 - \Omega_0) \right]^{-1/2} \quad (21)$$

(Fukugita et al. 1992). Figure 5 shows the angular diameter distances for the cosmological models considered in this paper. The distances depend on Ω_0 , λ_0 , and H_0 , but not σ_8 . The dependence upon λ_0 can be quite strong, which is why gravitational lenses can impose very stringent limits on the value of the cosmological constant (e.g. Fukugita et al. 1990; Kochanek 1996a).

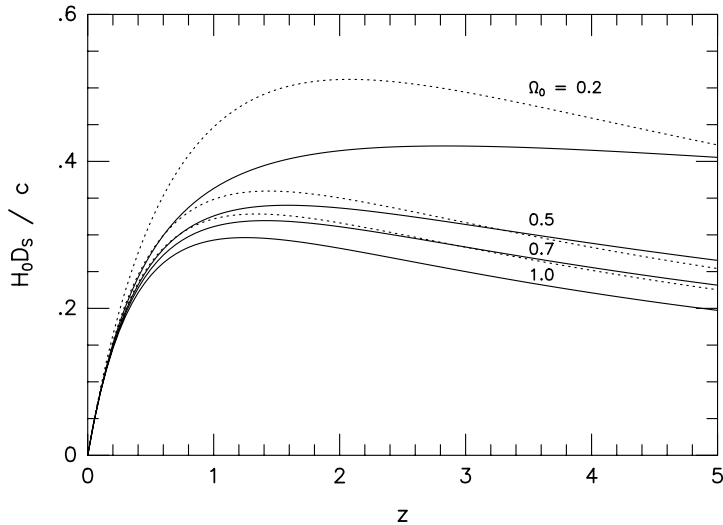


Figure 5: Angular diameter distance D_s in units of the Hubble radius c/H_0 , versus redshift z , for the various models considered in this paper. Solid curves: matter-dominated models ($\lambda_0 = 0$); dotted curves: flat, cosmological constant models ($\Omega_0 + \lambda_0 = 1$). Curves are labeled with the values of Ω_0 .

4.2. The Mean Background Density

The importance of gravitational lensing depends on the mean density of matter between the source and the observer, which is proportional to the present mean density of the universe,

$$\bar{\rho}_0 = \frac{3H_0^2\Omega_0}{8\pi G}. \quad (22)$$

The mean density depends on H_0 and Ω_0 , but not λ_0 and σ_8 .

4.3. The Large-Scale Structure

If the universe was perfectly homogeneous, there would be no gravitational lensing. It is the presence of density inhomogeneities, resulting from the growth of the large-scale structure, that is responsible for lensing. The amount of structure in the present universe is characterized by the parameter σ_8 . However, what is relevant is not the present large-scale structure, but the large-scale structure at redshift z_L corresponding to an angular diameter distance $D_L \simeq D_S/2$ where most of the matter responsible for lensing is located. Using linear perturbation theory, we can estimate the rms density fluctuation $\sigma_{8,L}$ at that redshift,

$$\sigma_{8,L} = \frac{\sigma_8}{\mathcal{L}(z_L, 0)}, \quad (23)$$

where $\mathcal{L}(z_L, 0)$ is the linear growth factor between redshifts z_L and 0, which depends on Ω_0 and λ_0 . Thus, $\sigma_{8,L}$ depends on σ_8 , Ω_0 , and λ_0 , but not H_0 . For the Einstein-de Sitter model, $\mathcal{L}(z, 0) = 1 + z$, hence σ_8 decreases monotonically with increasing z_L . For $\Omega_0 < 1$ models, the perturbation “freezes-out” at redshift $z_{\text{fr}} \sim 1/\Omega_0$, and grows very slowly between z_{fr} and the present. Hence, at fixed σ_8 , $\sigma_{8,L}$ increases with decreasing Ω_0 , and if $z_{\text{fr}} \gg z_L$, $\sigma_{8,L}$ should be comparable to σ_8 .

5. RESULTS

5.1. The Magnification Distributions

We compute the magnification distributions by combining all experiments within each cosmological model, and binning the cells on the magnification maps according to the value $\mu_{e,i}$ of the magnification in

each cell. We use magnification bins of equal width $\Delta\mu = 0.02$. The probability $P(\mu)\Delta\mu$ that a source has a magnification between μ and $\mu + \Delta\mu$ is given by

$$P(\mu)\Delta\mu = \frac{\sum_e n_e(\mu, \mu + \Delta\mu)}{\sum_e n_e(0, \infty)}, \quad (24)$$

where $n_e(\mu_1, \mu_2)$ is the number of cells in experiment e with magnification between μ_1 and μ_2 , and the sums are over the experiments. Notice that $n_e(0, \infty)$ is the number of cells for experiment e that are included in the analysis, which can vary among experiments (see discussion of Fig. 3). Equation (24) implies

$$\int_0^\infty P(\mu)d\mu = 1, \quad (25)$$

where the ‘‘integral’’ is actually a sum over bins. By substituting equation (18) into equation (24), we can easily show that

$$\int_0^\infty P(\mu)\mu d\mu = 1. \quad (26)$$

Equations (25) and (26) express the conservation of probability and the conservation of flux, respectively.

To estimate the accuracy of the distributions, we used a convergence criterion. The magnification and shear distributions were always updated each time new experiments were performed in a given model. We also computed, in each magnification bin, the uncertainty on the mean $\Delta P = \sigma/N_{\text{exp}}^{1/2}$, where σ is the standard deviation in that bin, and N_{exp} is the number of experiments included in the average. Eventually, we reached a point where adding new experiments did not change the distribution, in which case convergence has been achieved. For models with large Ω_0 , the convergence is reached much more slowly, and for a few models the especially large number of experiments done was still not sufficient to reach a tight convergence. We refer to models for which convergence has or has not been achieved as having ‘‘good statistics’’ or ‘‘poor statistics,’’ respectively, and we shall be careful when drawing conclusions for models which have poor statistics. In Figures 6–9, we compare the magnification distributions for various models. Error bars indicate the uncertainty ΔP on the mean (for clarity, we display error bars for only 1/4 to 1/3 of the bins). The important thing to point out is that the error bars are shorter than the separations between curves, except in regions where the curves are nearly identical. The differences between the various curves in Figures 6–9 are therefore real, and not a consequence of insufficient accuracy (except when stated otherwise).

5.1.1. The σ_8 Dependence

Figure 6 shows the magnification distributions for three different models with various combinations of Ω_0 , λ_0 , and H_0 . The various curves represent various values of σ_8 . For these models, we actually have results for 5 different values of σ_8 , but for clarity we only plot the distribution for the smallest, median, and largest values of σ_8 . In the absence of lensing, these distributions would be δ -functions centered at $\mu = 1$. These distributions reveal that most sources are slightly demagnified, few sources are strongly magnified, and the effect of lensing increases with increasing σ_8 . For the open and Λ models, we see a clear trend: as σ_8 increases, the peak of the distribution decreases, the low edge of the distribution moves to even lower values (more demagnification), but the right edge is hardly affected. We see a similar trend for the Einstein-de Sitter model, but more experiments are needed to improve the statistics. The explanation resides in the fact that the magnification is caused primarily by the matter located near the beam, whereas the matter located far from the beam is primarily responsible for the shear. Each lens plane contains a certain distribution of matter, with overdense and underdense regions. If the beam propagates through an underdense region, it will diverge, resulting in demagnification, and if it propagates through an overdense region, it will converge, resulting in magnification. In a cosmological model like CDM, structure formation proceeds hierarchically. Small structures form first, then merge to form bigger structures, which merge into even bigger structures, and so on. As time goes on, clusters become more massive and less abundant, and the voids between them become larger. A larger σ_8 implies that this hierarchical merging process is more advanced, and this affects the matter distribution in two ways: first, the underdense regions become more underdense and the overdense regions become more overdense, and second, the fraction of the plane covered by underdense

regions (the “filling factor”) increases while the fraction covered by overdense regions decreases. In the case of demagnification, these two effects act in the same direction: As σ_8 increases, the beam is more likely to propagate through an underdense region (because of the larger filling factor), and if it does, it will result in stronger demagnification, because these regions are more underdense. In the case of magnification, these effects act in opposite directions: as σ_8 increases, the beam is less likely to propagate through an overdense region, but if it does, the magnification will be stronger. As we see, these two effects are almost perfectly cancelling each other, and the distributions at values of $\mu > 1$ are essentially independent of σ_8 , at least for the open and Λ models. For the Einstein-de Sitter model, the statistics are poor, even though we performed significantly more experiments for this model than the other ones.

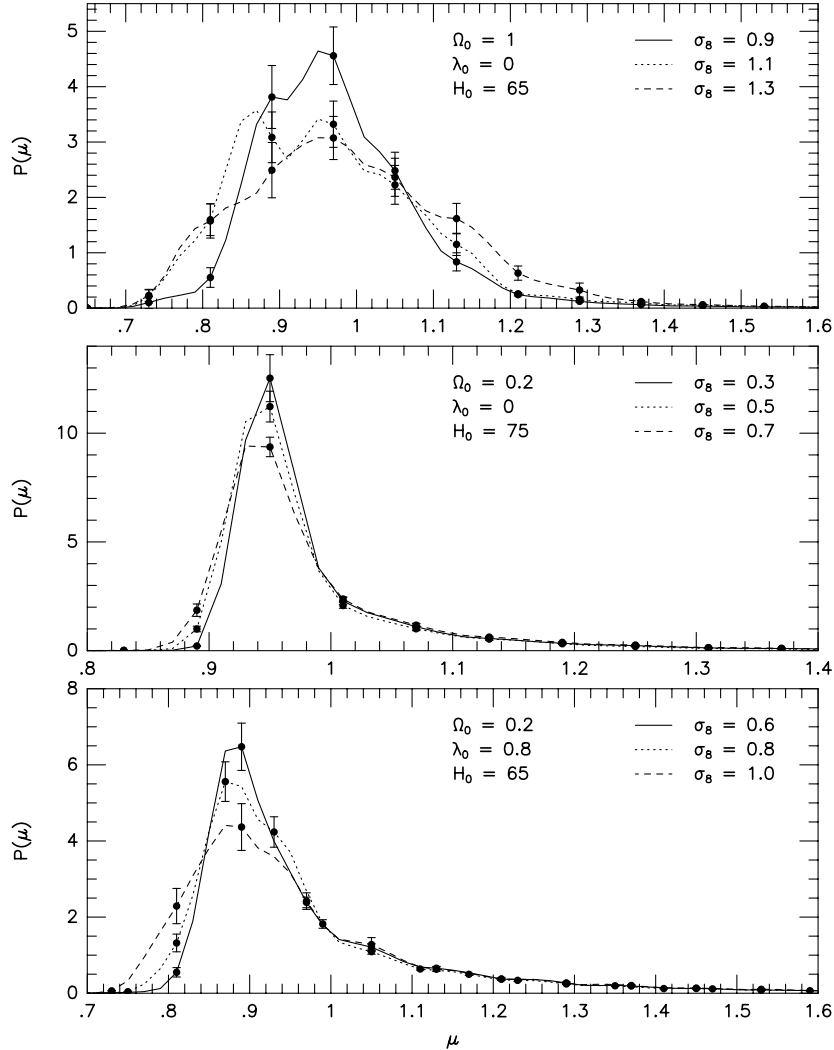


Figure 6: Magnification distributions for various combinations of Ω_0 , λ_0 , and H_0 , showing the effect of varying σ_8 . Error bars indicate the $1 - \sigma$ uncertainty ΔP on the mean, for a few representative bins. See text for details.

5.1.2. The H_0 Dependence

Figure 7 shows the magnification distributions for three different models with various combinations of Ω_0 , λ_0 , and σ_8 . The various curves represent various values of H_0 . For the Einstein-de Sitter model (top panel) and Λ -model (bottom panel), the distributions become narrower as H_0 increases (the distributions of the top panel are quite noisy, but if one focuses on the ordering of the curves along the left edge of the distribution, the trend becomes clear). This trend was expected, since the cosmological distances are shorter

in models with large H_0 , resulting in a weakening of the effect of gravitational lensing. Notice that this effect is partially compensated by the fact that at fixed Ω_0 , the mean background density increases like H_0^2 . From the point of view of the algorithm, a model with larger H_0 has a *smaller number* of denser lens planes between the source and the observer. For the open model (middle panel), these two effect almost perfectly cancel each other, and the distributions are essentially independent of H_0 .

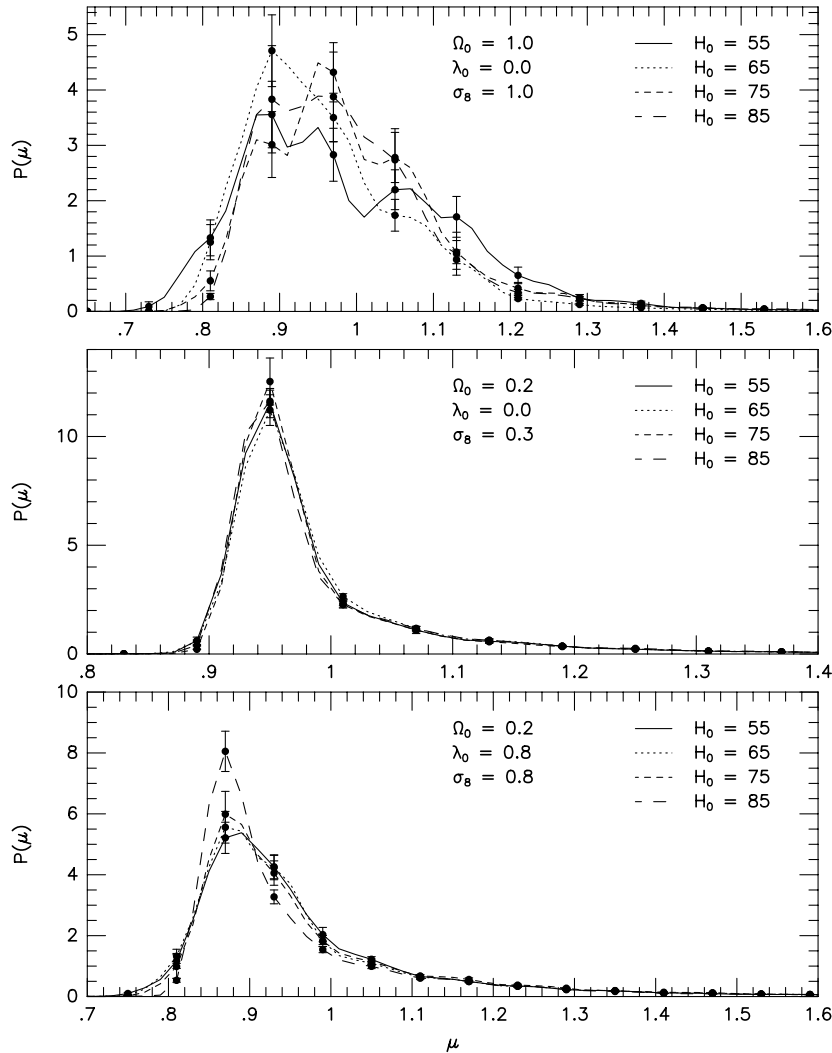


Figure 7: Magnification distributions for various combinations of Ω_0 , λ_0 , and σ_8 , showing the effect of varying H_0 . Error bars indicate the $1 - \sigma$ uncertainty ΔP on the mean, for a few representative bins. See text for details.

5.1.3. The Ω_0 Dependence

Figure 8 shows the magnification distributions for two different models with various combinations of λ_0 , H_0 and σ_8 . The top panel shows matter-dominated models ($\lambda_0 = 0$), while the bottom panel shows flat models ($\Omega_0 + \lambda_0 = 1$). The various curves represent various values of Ω_0 . Of all the various dependences, the Ω_0 dependence is the most difficult one to interpret. The reason is that Ω_0 is the only parameter which all elements of lensing, distance, mean background density, and structures, depend on. We are therefore dealing with three concurrent effects. As Ω_0 increases, the mean background density increases, favoring stronger lensing effects. However, the cosmological distances decrease, favoring weaker lensing effects, and at fixed σ_8 , the large-scale structure at high-redshift is less developed because freeze-out occurs later, also favoring weaker lensing effects. For matter-dominated models (top panel), the importance of lensing increases with

Ω_0 , resulting in a shift of the distribution toward lower values. The dominant effect in this regime is therefore the mean background density. The bottom panel shows the magnification distributions for flat models, with λ_0 increasing as Ω_0 decreases. As Figure 5 shows, at redshifts $z \leq 3$ the angular diameter distances increase with λ_0 for all models, and this reinforces the dependence upon Ω_0 . The distances get even larger with smaller Ω_0 , and this helps overcoming the mean background density effect. The bottom panel in Figure 8 shows that, in the limit of large λ_0 , the effect of having large distances dominates over competing effects. However, for values $\Omega_0 \geq 0.5$ (or $\lambda_0 \leq 0.5$), there is no clear dependence of the magnification distribution on Ω_0 , and we would need much better statistics to determine whether there is an effect. In any case, the effect would probably be quite small.

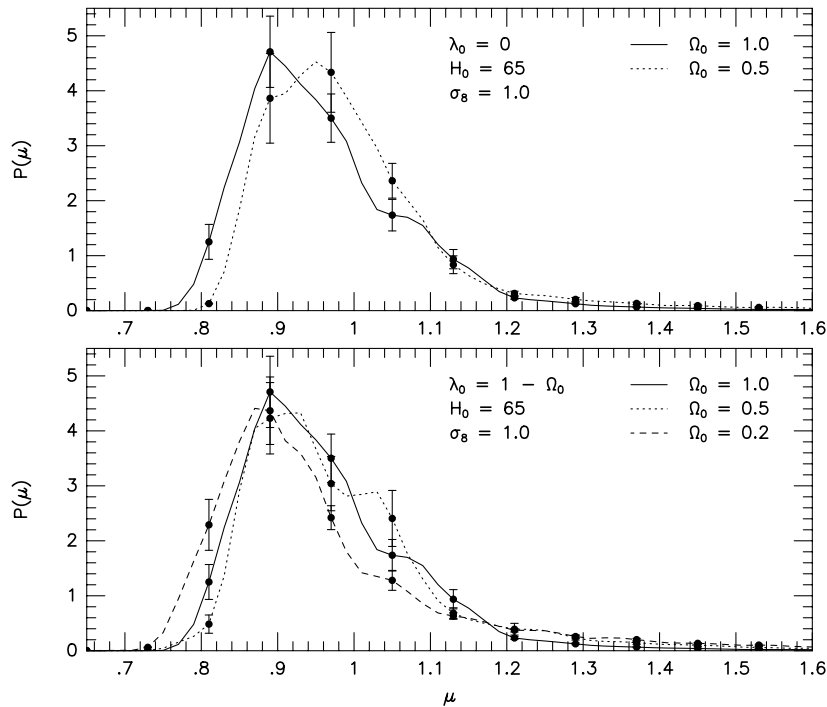


Figure 8: Magnification distributions for various combinations of λ_0 , H_0 , and σ_8 , showing the effect of varying Ω_0 . Error bars indicate the $1 - \sigma$ uncertainty ΔP on the mean, for a few representative bins. See text for details.

5.1.4. The λ_0 Dependence

Figure 9 shows the magnification distributions for two different models with various combinations of Ω_0 , H_0 , and σ_8 . The various curves represent various values of λ_0 . The presence of a cosmological constant increases the effect of magnification by increasing the cosmological distances. For the low-density model ($\Omega_0 = 0.2$, top panel), the cosmological constant results in a widening of the distribution, and a shift toward lower magnifications. The effect is much less important for the $\Omega_0 = 0.5$ model (bottom panel). This indicates that the effect of the cosmological constant is small for values $\lambda_0 \leq 0.5$, and becomes important only for larger values. As Figure 5 shows, the effect of λ_0 on the angular diameter distances is relatively small for models with $\Omega_0 \geq 0.5$ (or $\lambda_0 \leq 0.5$), but the difference between the $\Omega_0 = 0.2$, $\lambda_0 = 0$, and the $\Omega_0 = 0.2$, $\lambda_0 = 0.8$ models is very large.

5.1.5. Large-Scale Structure versus Galaxies

In our simulations, the density inhomogeneities responsible for lensing consists of the large-scale structure of the universe and the galaxies that are embedded inside that structure. Including large-scale structure and galaxies in the algorithm enables us to study both the effect of weak and strong lensing. While most of

the weak lensing results from the presence of the large-scale structure, the rare, high-magnification events usually result from the presence of a massive galaxy along the line of sight. One may wonder if strong lensing is affected by the cosmological parameters, σ_8 in particular. This parameter measures the amplitude of the density fluctuations in the large-scale structure, but since the algorithm chooses galaxy locations according to the background density, galaxies are more clustered in models with a larger σ_8 . This does not change the probability that a given source will be lensed by a galaxy, but it could increase the probability of a source being lensed by two or several galaxies clustered together, resulting in a very large magnification. Lensing by multiple galaxies must be invoked to explain the properties of some of the images (see Fig. 13 below). However, the high-tail of the magnification distributions shown in Figure 6 appears to be independent of the value of σ_8 . In particular, we do not find the dramatic increase in the values of μ with higher σ_8 that one would expect if sources are lensed by compact groups of galaxies.

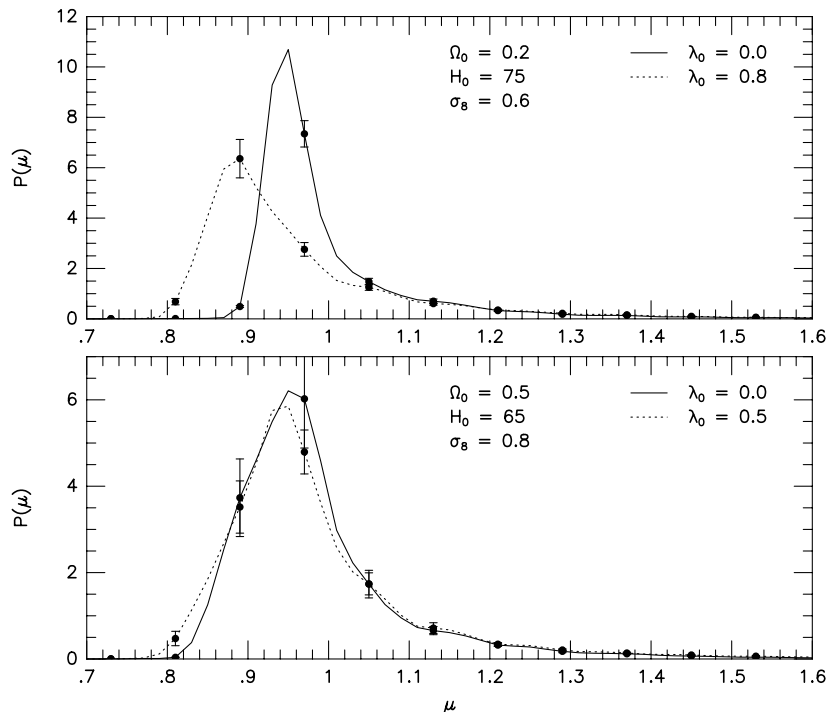


Figure 9: Magnification distributions for various combinations of Ω_0 , H_0 , and σ_8 , showing the effect of varying λ_0 . Error bars indicate the $1 - \sigma$ uncertainty ΔP on the mean, for a few representative bins. See text for details.

We investigate this question by estimating the likelihood that a source will be lensed by two galaxies on the same lens plane. Our algorithm models galaxies as truncated isothermal spheres with a mass-dependent radius r_{\max} given by equation (7). We computed the geometric cross section πr_{\max}^2 for all galaxies, and added them up, to find out what fraction f_{gal} of the lens plane is covered by galaxies. For lens planes located near $z = 0$, we obtain $0.00326 \leq f_{\text{gal}} \leq 0.00503$ (the value depends on H_0 ; see comment following eq. [4]). Hence, only a small fraction of the plane is covered by galaxies. However, for sources at $z = 3$, the lensing is caused primarily by planes located near $z = 1$. Since at $z = 1$ the planes are smaller but the galaxies have the same size,¹⁴ we gain a factor $(1 + z)^2 = 4$, and the fraction covered by galaxies is then in the range $0.013 \leq f_{\text{gal}} \leq 0.020$, still quite small. Galaxy clustering will create regions where the covering is larger. If we assume that clustering could increase the space density of galaxies in some regions by a factor of 1000 (quite optimistic at $z = 1$), the surface density would go up by 100, and there could be some galaxies overlapping.

¹⁴ Our current algorithm neglects galaxy evolution, and assumes that the galaxy parameters given by equations. (6)–(8) are independent of redshift.

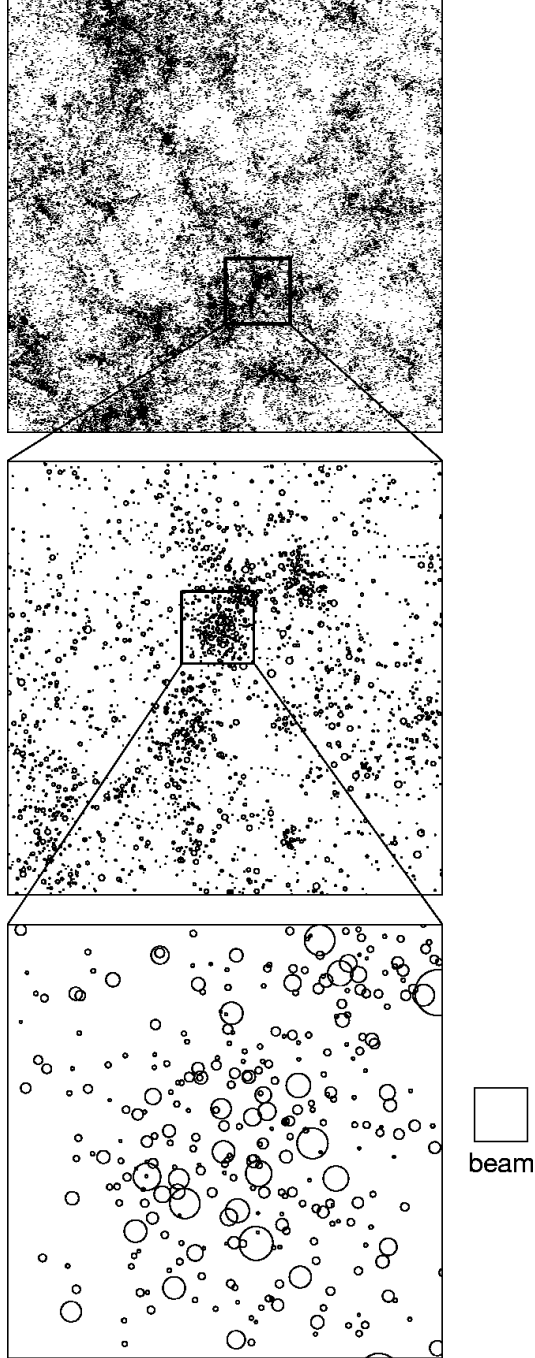


Figure 10: Top panel: Galaxy distribution at $z = 0.964$ for $\Omega_0 = 0.2$, $\lambda_0 = 0.8$, $H_0 = 65 \text{ km s}^{-1} \text{ Mpc}^{-1}$, $\sigma_8 = 0.8$ model. Each galaxy is represented by a dot. Middle panel: enlargement of a galaxy-rich region. Bottom panel: enlargement of a rich cluster of galaxies. Galaxies in the middle and bottom panels are represented by circles of radius r_{max} , as defined by equation (7).

Figure 10 shows the galaxy distribution on a lens plane located at $z = 0.964$, for the model $\Omega_0 = 0.2$, $\lambda_0 = 0.8$, $H_0 = 65 \text{ km s}^{-1} \text{ Mpc}^{-1}$, $\sigma_8 = 0.8$. The top panel shows the galaxy distribution over the entire lens plane, with galaxies represented as dots. Because of freeze-out, the galaxies at that redshift are almost as clustered as at redshift $z = 0$. We zoom-in on one of the densest, most galaxy-rich region, and display that region in the middle panel of Figure 10, where galaxies are now represented as circles with radii equal

to r_{\max} . Because the galaxies follow a Schechter distribution, most galaxies have small radii and few have large radii. We zoom-in on the richest galaxy cluster in this region, and display it in the bottom panel of Figure 10. There are some galaxies overlapping, but not many. The beam, displayed next to the bottom panel of Figure 10, is larger than the galaxies at that redshift, so it might hit several galaxies, but the light coming for one individual cell in the beam is unlikely to hit more than one galaxy, in spite of the fact that galaxies are strongly clustered in this region. Of course, we have considered only one plane. A light ray can hit a galaxy on one plane, and then another galaxy on another plane. But since the structures on neighboring planes are uncorrelated, the probability of occurrence of such double hit is unaffected by clustering. The high tail of the magnification distributions depends on the distribution of galaxy properties (masses, truncation radii, core radii), but not on their actual locations or level of clustering.

5.2. The Magnification Probability

The magnification probability is defined as

$$P_m = \int_1^{\infty} P(\mu) d\mu. \quad (27)$$

In a large, representative region of the sky, P_m represents the fraction of sources that are magnified. In Figure 11, we plot P_m vs. σ_8 , for all models. We do not find any particular trend. Instead, P_m is essentially independent of σ_8 . This could have been anticipated from Figure 6, which showed that for most models, $P(\mu)$ is independent of σ_8 in the integration range of equation (27). However, this result is in conflict with the argument we presented in §5.1.1. We argued that as σ_8 increases, the filling factor of overdense regions decreases, so a particular source is less likely to be magnified, but if it is, the magnification will be larger. However, P_m measures the fraction of sources that are magnified, and does not depend upon how large the magnifications are. Hence, according to this argument, P_m should simply be a measure of the filling factor of overdense regions, and therefore should decrease with increasing σ_8 at fixed Ω_0 , λ_0 , and H_0 . We do not see this trend in Figure 11. We even see the opposite trend (P_m increasing with σ_8) in a few cases, such as $\Omega_0 = 1$, $\lambda_0 = 0$, $H_0 = 65 \text{ km s}^{-1} \text{ Mpc}^{-1}$ (open triangles in bottom panel). This shows that the interpretation of the magnification distributions in terms of filling factors of overdense and underdense regions might be sufficient to explain the properties of $P(\mu)$ for $\mu < 1$, as we did in §5.1.1, but is too simplistic in the regime $\mu > 1$.

The basic flaw in this argument is the assumption that P_m depends only on whether or not sources are magnified (by having the beam going through a high-density region), and not by how much. If there was only one lens plane between the source and the observer, this argument would be correct: P_m would be equal to the filling factor of the overdense regions on that plane. However, there are many planes, and even though there is an optimal redshift z_L where most of the matter responsible for lensing is located, there should be several planes at redshift $z \sim z_L$ that contribute to lensing significantly. Suppose that the light coming from a source hits a high-density region on plane i and then a low-density region on plane j . Plane i will magnify the source and plane j will demagnify it. Whether the demagnification caused by plane j is sufficient to bring the value of μ below unity will depend on how large the magnification by plane i was. For small values of σ_8 , the filling factor of overdense regions on plane i is large, and many sources are magnified, but they are only slightly magnified ($\mu \gtrsim 1$), and the demagnification caused by plane j will bring many of these sources down to $\mu < 1$. With larger σ_8 , fewer sources are magnified, but they are magnified to larger values of μ , and more of them can “survive” the demagnification caused by plane j . This can also be regarded as a consequence of the absence of correlation between planes. Increasing σ_8 increases the density contrast on each plane, but by stacking uncorrelated planes along the line of sight, the resulting mean density contrast is much smoother than the density contrast on any individual plane, and the effect of increasing σ_8 is mostly averaged-out.

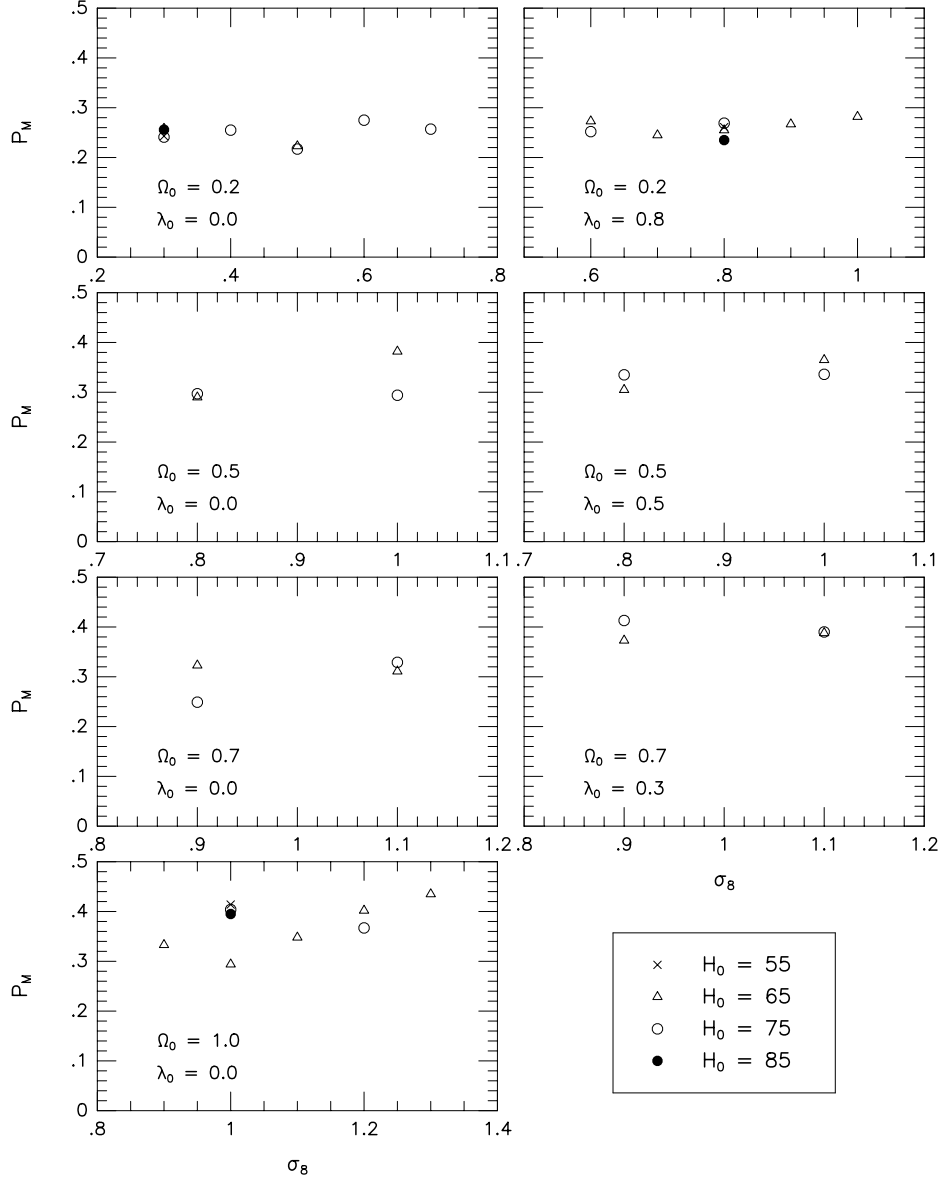


Figure 11: Magnification probability P_m vs. σ_8 . The values of Ω_0 and λ_0 are indicated in each panel. The various symbols correspond to various values of H_0 .

The only significant trend we found is that P_m increases with Ω_0 , as shown in Figure 12. In spite of the large scatter, the trend is significant. For $\Omega_0 = 0.2$, P_m is between 0.2 and 0.3, while for $\Omega_0 = 1$, P_m is larger than 0.29 for all models, with a mean value of order 0.36. The dependence of the distances upon Ω_0 is probably responsible for this effect. As Ω_0 goes up, the distances become shorter, and correspondingly there are fewer lens planes near $z \sim 1$, reducing the “averaging-out” of the density contrast discussed above.

Figure 12 shows that for $\Omega \leq 0.5$, P_m does not seem to depend upon λ_0 . For $\Omega_0 = 0.7$, however, P_m is significantly larger for $\lambda_0 = 0$ models than $\lambda_0 > 0$ models. This is very strange, since the $\lambda_0 = 0$ models and flat models resemble each other more closely as Ω_0 increases. This effect is probably spurious, a consequence of poor statistics. As Ω_0 increases, more experiments must be performed in order to obtain good statistics. This was our motivation for performing a large number of experiments for the Einstein-de Sitter model. However, we did not performed a particularly large number of experiments for the $\Omega_0 = 0.7$ models, which we regard as the least interesting models presented in this paper.

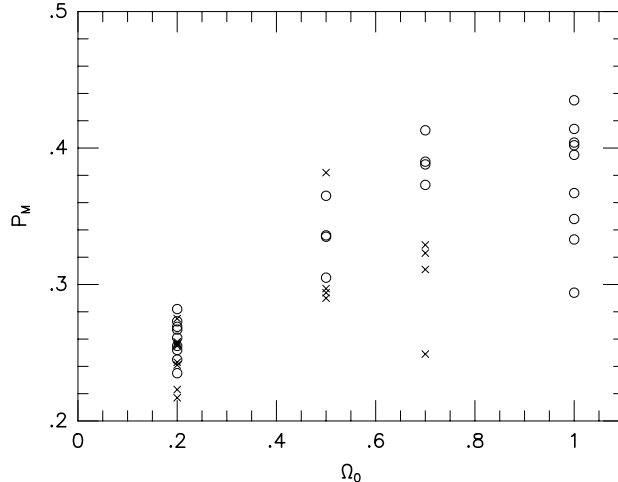


Figure 12: Magnification probability P_m vs. Ω_0 . Open circles: flat models (including Einstein-de Sitter); crosses: open models.

5.3. Classification of the Images

In Figure 13, we plotted, for illustration purpose, some of the images we have encountered. Each panel shows the image of a single circular source of angular diameter $1''$. We have plotted the location of the light rays on the image plane, and enlarged the dots representing these rays until the images look continuous. Individual rays can be seen along the edges of the images. In the absence of lensing, each image would be circular and would contain 190 light rays.

Figure 13a shows the most common case: a single image, magnified and sheared. In such case, there is no galaxy along the line of sight. The magnification is caused by the background matter located near the beam, while the shear is mostly caused by the background matter and galaxies distant from the beam. Figures 13b and 13c illustrate the two most common cases of double image. Figure 13b shows a case of strong lensing. In such cases, the magnification is always large, in the range $\mu = 3 - 7$, the brightness ratio between the bright image and the faint one is small, of order of a few, and the brightest image forms an arc, while the faintest image is more compact and invariably shows a spike that points toward the other image. This is a consequence of the particular density profile we assume for galaxies (eq. [5]). Figure 13c is a case of weak lensing. In such cases, the magnification is small, of order $\mu = 1.2 - 1.3$, and the brightness ratio is very large. The effect of lensing is to “carve” a second, faint image out of the brighter one. Figure 13d shows an Einstein ring, caused by a lensing galaxy nearly aligned with the source. For such rings, the magnification is always very high, sometimes larger than 10. Figure 13e shows a very different, and unusual, Einstein ring. The ring is pinched at two different locations, where the width is only one light ray, and the magnification is quite small, less than 2. This case is actually similar to the double image case shown in Figure 13c, and one can go from one case to the other continuously by shifting the location of the source. Figures 13f–13h show cases of triple image. The images can form either a circular pattern (as in Fig. 13f), in which case the brightness ratios between the images are small, or a linear pattern (as in Figs. 13g and 13h), in which case one image is usually much brighter than the other two, that image being located either in the middle, as in Figure 13g, or on the edge, as in Figure 13h. The latter one is similar to some triple images generated by Makino & Tomita (1995, their Figs. 6b and 6d). Figures 13i and 13j show cases of quadruple image. These cases suggest that several galaxies are involved in the lensing. Figure 13k shows an interesting case of a double image, one of them being a ring. This is actually a combination of the cases shown in Figures 13b and 13d. There are two galaxies near the line of sight, one responsible for forming the ring, and the other responsible for forming the second image. Figure 13l shows a very rare case of an Einstein ring with two holes. This requires an alignment between the source and 2 intervening galaxies, each of them producing a hole. Figures 13m and 13n show even rarer cases of an Einstein ring with 2 holes and a secondary image, and an Einstein ring with 3 holes, respectively. We have encountered only one of each of these cases in all of our experiments.

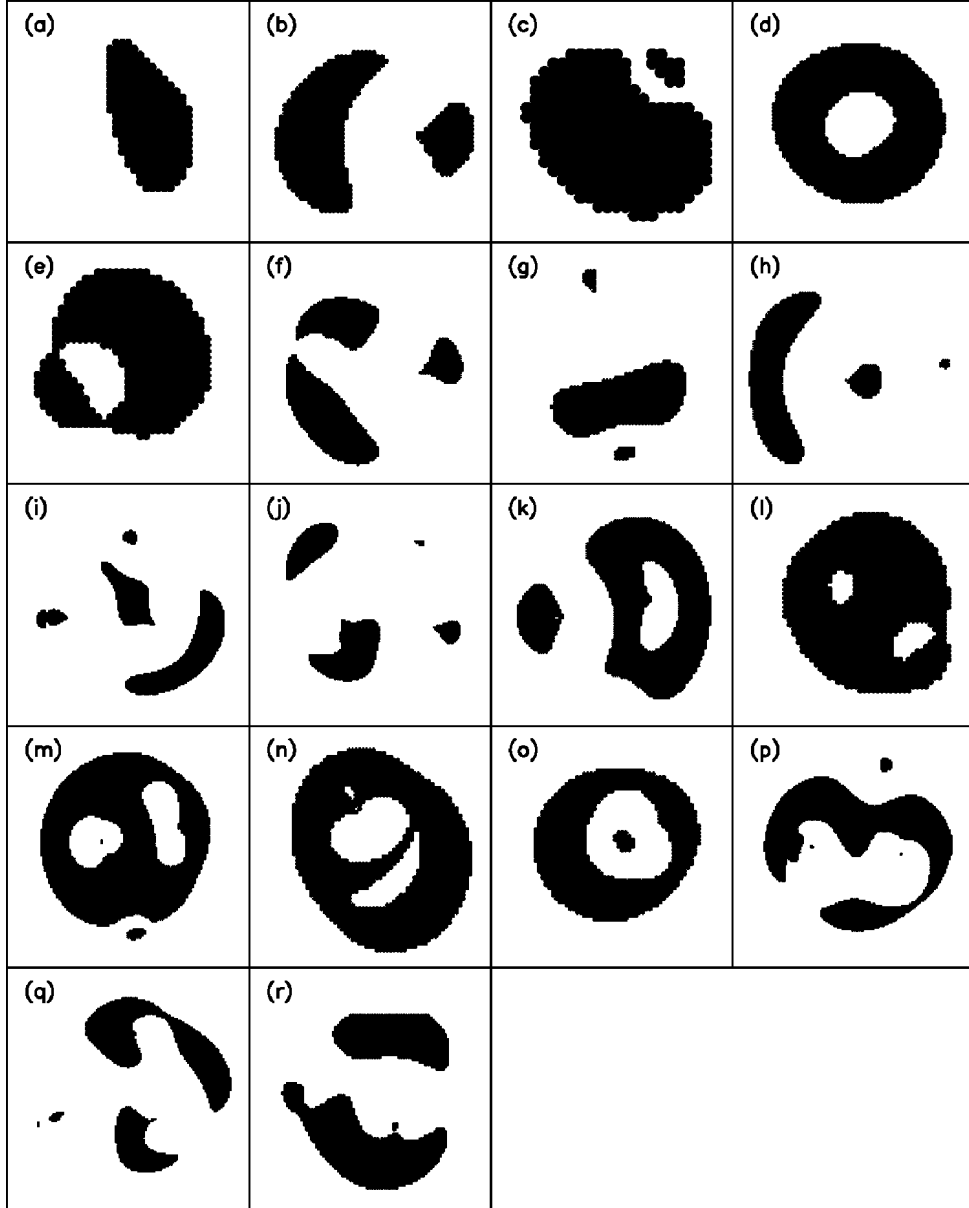


Figure 13: Images of lensed circular sources, for a few interesting cases: (a) single image; (b) and (c) double image; (d) and (e) Einstein ring; (f), (g), and (h) triple image; (i) and (j) quadruple image; (k) Einstein ring with secondary image; (l) double Einstein ring; (m) double Einstein ring with secondary image; (n) triple Einstein ring; (o) Einstein ring with central image; (p), (q), and (r) complex images caused by multiple lensing.

Figure 13o shows an Einstein ring with a central spot. The presence of this spot is a consequence of the particular model we use for the galaxies. We do not represent galaxies as singular isothermal spheres, but rather as nonsingular isothermal spheres with a central core. Such objects can produce three images if the angular separation between the object and the source is sufficient small (see SEF, pp. 244 and 396, and §5.5.1 below). In this case, the three images are located on the line going through the source and the lens on the celestial sphere, one image on each side of the lens, and the third image in the core of the lens. If the lens and the source are aligned, there are no preferred directions, and the two outer images will turn into a ring, while the third image, located in the core of the galaxy, will form a “spot.” This explains the existence of images like the one displayed in Figure 13n, but it does not explain the existence of rings *without* spot,

such as the one displayed in Figure 13d. In our experiments, less than 1% of the rings have a central spot. This is simply a resolution effect. As SEF point out, for lenses modeled as nonsingular isothermal sphere, the third image, located in the core, is very faint. If the brightness of that image is less than one light ray, we cannot resolve it. Indeed, we often found rings containing a spot composed of less than five rays, which we regarded as being underresolved.

Finally, in Figures 13p–13r, we plotted some of the strangest images we encountered. These complex images result from lensing by several galaxies, combined with shear caused by the background matter.

The reader should keep in mind that most of these cases are extremely rare. 99.7% of the images fall in the category illustrated by Figure 13a, a single image, magnified and sheared. Of the remaining cases, the vast majority of them fall in the categories illustrated by Figures 13b–13d. The cases shown in Figures 13e–13r are all very rare. In §5 we will discuss in more detail the probability of occurrences of these various cases.

5.4. The Shear Distributions

There are several ways to compute the shear caused by gravitational lensing. The most direct way is to compute iteratively the magnification matrix along each light ray (SEF, §9.1.2), and compute its eigenvalues. This approach is not very practical for our experiments. We consider beams composed of light rays separated by $0.064''$. The magnification matrix would tell us the properties (rotation and deformation) of a source having that size. We are, however, considering sources of angular diameter $1''$, containing, in the absence of magnification, 190 light rays. We could always try to somehow combine the magnification matrices for all the rays inside an image to infer its properties, but there is a much simpler approach. Since we are actually resolving the shapes of individual images, we can estimate the shear simply by computing the aspect ratio of the images.

To compute the aspect ratio of an image, we first compute the geometrical center of the image on the image plane,

$$\mathbf{r}_{\text{gc},i} = \frac{1}{N_i} \sum_k \mathbf{r}_{k,i}, \quad (28)$$

where $\mathbf{r}_{k,i}$ is the location of light ray k in image i , and N_i is, as usual, the number of rays in image i . We then compute the 2-dimensional quadrupole tensor of the image,

$$\mathbf{Q} = \sum_k (\mathbf{r}_{k,i} - \mathbf{r}_{\text{gc},i})(\mathbf{r}_{k,i} - \mathbf{r}_{\text{gc},i}) = \begin{bmatrix} A & B \\ B & C \end{bmatrix}, \quad (29)$$

where the last equality defines the components A , B , C . The aspect ratio of the image is obtained from the eigenvalues λ_1 , λ_2 of \mathbf{Q} , as follows,

$$\frac{a_1}{a_2} = \left\{ \frac{[A + C + [(A - C)^2 + 4B^2]^{1/2}]}{[A + C - [(A - C)^2 + 4B^2]^{1/2}]} \right\}^{1/2}. \quad (30)$$

where a_1 and a_2 are the long and short “axes” of the image. One interesting property of this expression is that in the case of an elliptical image, a_1 and a_2 are the semi-major and semi-minor axes of the ellipse, respectively. The resulting shear distributions are plotted in Figures 14–17. Error bars have the same meaning as in Figures 6–9.

5.4.1. The σ_8 Dependence

Figure 14 shows the shear distributions for models with the same values of Ω_0 , λ_0 , and H_0 , and different values of σ_8 . In the absence of lensing, the distributions would be δ -functions located at $a_1/a_2 = 1$. As for the magnification distributions, the larger the departure from a δ -function is, the stronger the effect of lensing is. The top panel shows various Einstein-de Sitter models with different values of σ_8 . As σ_8 increases, the peak of the distribution decreases while the high-tail of the distribution increases. This was expected, since the large-scale structure, whose amplitude is measured by σ_8 , is the primary origin of the

shear. Interestingly, the distributions are much less sensitive to the value of σ_8 for the other models. For the $\Omega_0 = 0.2, \lambda_0 = 0$ model, the curves in the high-tail regions are very similar and cross each other several times, while for the $\Omega_0 = 0.2, \lambda_0 = 0.8$ model the cases $\sigma_8 = 0.8$ and $\sigma_8 = 1.0$ are almost undistinguishable. Therefore, the dependence of the shear distribution upon σ_8 is more pronounced for models with large Ω_0 . We found a similar trend in Figure 6 for the magnification distributions.

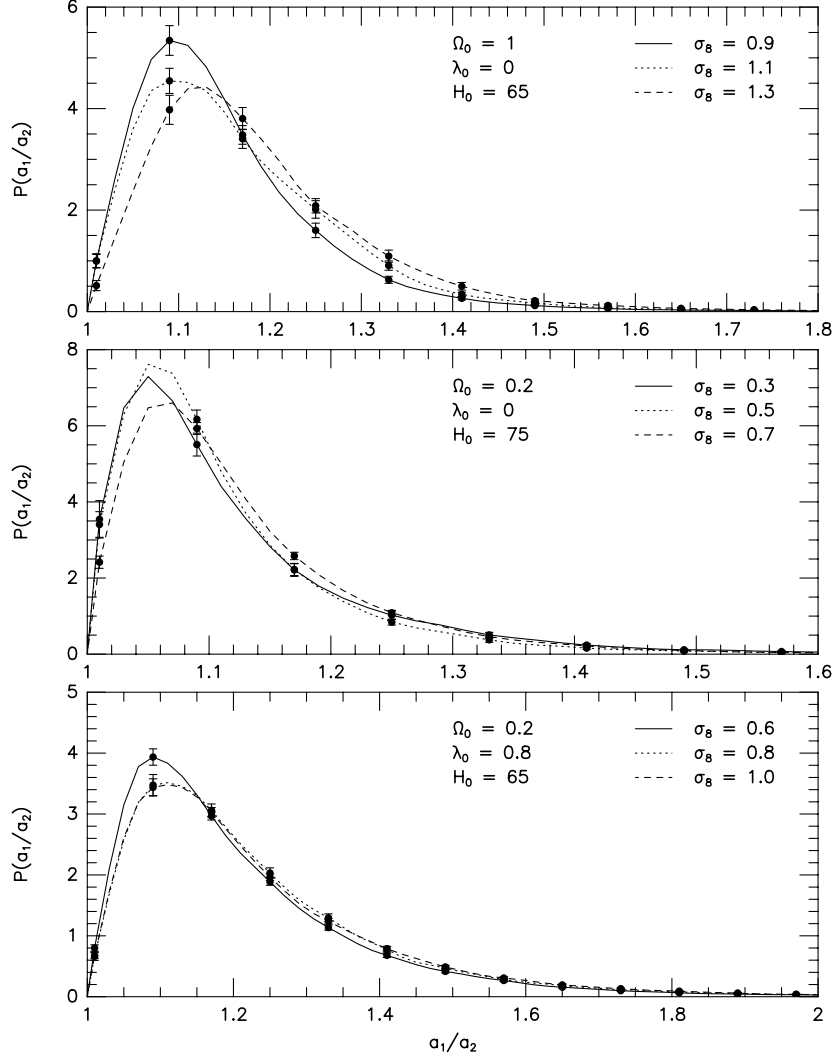


Figure 14: Distributions of aspect ratios for various combinations of Ω_0 , λ_0 , and H_0 , showing the effect of varying σ_8 . Error bars indicate the $1 - \sigma$ uncertainty ΔP on the mean, for a few representative bins. See text for details.

5.4.2. The H_0 Dependence

Figure 15 shows the shear distributions for models with the same values of Ω_0 , λ_0 , and σ_8 , and different values of H_0 . The curves in each panel are very similar, except for the case $H_0 = 55 \text{ km s}^{-1} \text{ Mpc}^{-1}$ in the top panel, for which the statistics are poor. We do not find any particular trend, and the ordering of the curves with H_0 is not even monotonic. As for the magnification distributions shown in Figure 7, the absence of dependence upon H_0 results from competing effects. With larger H_0 , the mean background density is higher, increasing the effects of lensing, but the cosmological distances are shorter, decreasing the effects of lensing.

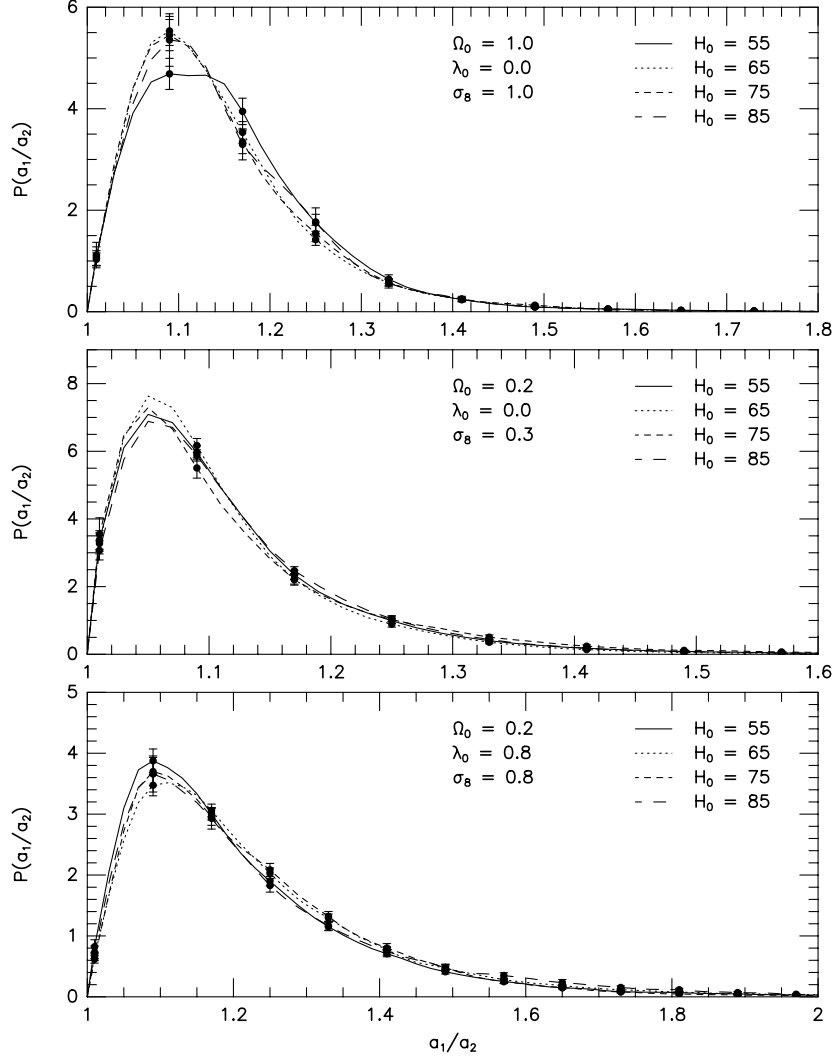


Figure 15: Distributions of aspect ratios for various combinations of Ω_0 , λ_0 , and σ_8 , showing the effect of varying H_0 . Error bars indicate the $1 - \sigma$ uncertainty ΔP on the mean, for a few representative bins. See text for details.

5.4.3. The Ω_0 Dependence

The top panel of Figure 16 shows the shear distributions for two matter-dominated models ($\lambda_0 = 0$) with the same values of H_0 and σ_8 , and different values of Ω_0 . This situation is similar to the one encountered in §5.1.3 for the magnification distributions. All elements of gravitational lensing — cosmological distances, mean background density, large-scale structure — depend upon Ω_0 , but the dependence upon the mean background density dominates, and consequently the distribution is wider (that is, lensing is stronger) for models with larger Ω_0 . The bottom panel of Figure 16 shows comparisons between flat models ($\Omega_0 + \lambda_0 = 1$). This is a totally different situation. As Ω_0 decreases, λ_0 increases, and the dependence of the cosmological distances upon λ_0 becomes the dominant effect, resulting in stronger lensing for models with smaller Ω_0 .

5.4.4. The λ_0 Dependence

Figure 17 shows the shear distributions for two models with the same values of Ω_0 , H_0 , and σ_8 , and different values of λ_0 . As λ_0 increases, the distributions become wider, indicating that the effect of lensing is stronger. A larger value of λ_0 results in larger cosmological distances, which is clearly the dominant effect

here. The effect of introducing a finite value λ_0 is very large for the $\Omega_0 = 0.2$ model, but becomes weaker for larger values of Ω_0 , as the flat and open models become more similar.

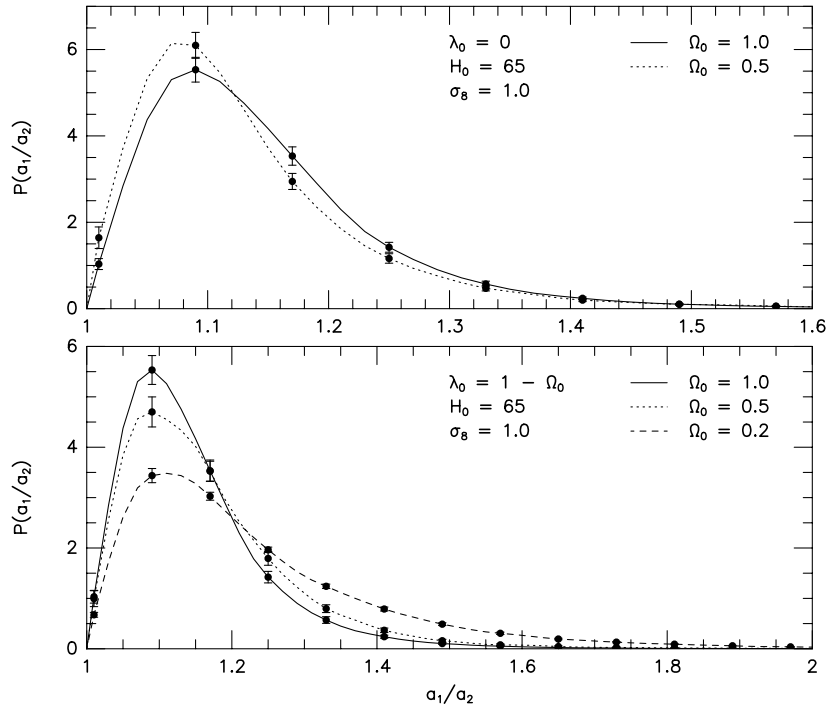


Figure 16: Distributions of aspect ratios for various combinations of λ_0 , H_0 , and σ_8 , showing the effect of varying Ω_0 . Error bars indicate the $1 - \sigma$ uncertainty ΔP on the mean, for a few representative bins. See text for details.

5.4.5. Large-Scale Structure versus Galaxies

All results presented in this section are consistent with the ones presented in §5.1. The magnification distributions and shear distributions have the same, or similar, dependences upon the cosmological parameters. This strongly suggests that magnification and shear are two different manifestations of one single physical phenomenon: weak lensing. In §5.1.5, we argued that the effect of galaxies on the magnification distributions is small, because galaxies cover only a small fraction of the lens planes. For the shear distributions, the situation is different. While magnification is primarily caused by the matter located near the beam, shear is primarily caused by the matter located away from the beam. In this case, the cross section of galaxies becomes irrelevant. The lack of contribution to the shear from galaxies comes from two different effects. First, even for the lowest mean background densities we consider, $\Omega_0 = 0.2$, the galaxies account for only 24% of the total mass. Second, as explained in great details in Paper I, each galaxy in the simulation resides on top of an extended, smooth, compensating “hole” of negative density, which is introduced to account for the matter that has been removed from the intergalactic medium to form this galaxy in the first place. This is necessary, otherwise the process of “adding” galaxies to the simulation would not conserve mass.¹⁵ As a result, the total mass galaxy + “hole” is zero, and galaxies have no influence beyond the radius of the hole, which we fixed at $r_{\text{hole}} = 1 \text{ Mpc}$. Hence, only the (usually) small fraction of galaxies which are located within 1 Mpc of the beam can contribute to the shear.

¹⁵ This is an improvement over the approach used by Jaroszyński (1991), which involved an overall, uniform reduction of the mean background density.

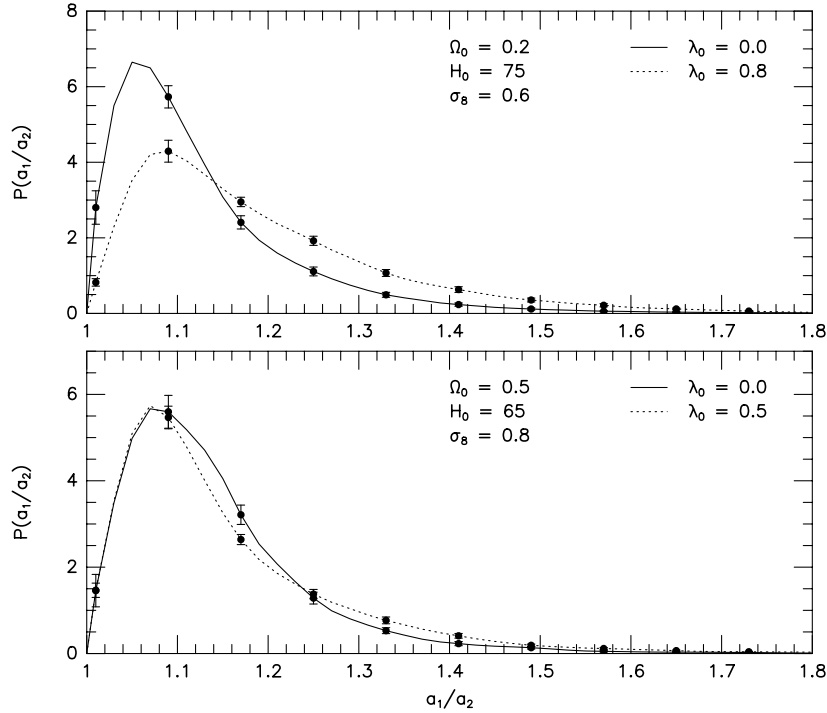


Figure 17: Distributions of aspect ratios for various combinations of Ω_0 , H_0 , and σ_8 , showing the effect of varying λ_0 . Error bars indicate the $1 - \sigma$ uncertainty ΔP on the mean, for a few representative bins. See text for details.

5.5. The Multiplicity of Images

5.5.1. Practical Considerations

For all cases of multiple images found in our experiments, we have computed the image separations, defined as the angular separation between the center of the images. In doing so, we had to decide which cases should actually be identified as multiple images. We have designed an algorithm with pattern recognition capability to automatically identify multiple images and compute their separations, as well as the brightness of each image. It turns out that in a very large number of cases, one of the images contains only one or two rays. In such cases, that image is demagnified by a factor of 100, and the brightness ratio between the two images is of order of 100 or more. It is extremely doubtful that an observer could resolve such a faint image. Indeed, as we will argue in §5.5.2 below, the vast majority of observed gravitational lenses probably contain an unresolved image.

To keep the number of cases with multiple images at a manageable level, we excluded from this study all images containing less than 5 light rays. Therefore, a double image with one image containing less than 5 rays is treated as a single image, a triple image is treated as a double image, and so on. By imposing this restriction, we are postulating that an image with less than 5 rays could never be resolved. However, we are not assuming that an image with 5 rays or more is resolvable. The 5-ray limit was introduced mostly for convenience, to facilitate the analysis, but as we will show in §5.5.2 below, the number of double images we predict is much too large to agree with observations, indicating that a realistic cutoff would have to be much larger than 5 rays.

5.5.2. Theory, Simulations, and Observations

We define P_n as the probability that a randomly selected source will have n images. In our experiments, each cell on the source plane is a potential location for a source, and cells are given equal probability. To compute P_n we simply divide the number of cases with n images by the total number of cells included in the analysis. We have performed a total of 3,798 experiments. For most experiments, 841 cells are included

in the analysis. In some cases, however, cells located near the edge of the beam must be rejected (see §3.3). Combining all experiments for all models, we have a total of 3,137,675 cells, each of them representing a potential source. Excluding any image that is composed of less than 5 rays, we found 10,728 double images, 126 triple images, and 6 quadruple images. No cases with five images or more were found. This contradicts the *odd-number theorem* (SEF, p. 172, Theorem 1), as well as observations, which find $N_2 \sim N_4 \gg N_3$ (Kochanek et al. 1998). This is a consequence of limited resolution. In most realistic lens models, whenever multiple images are produced, one image is always very faint (see, e.g., SEF, pp. 58 and 175), often too faint to be observed. Furthermore, for lens models such as nonsingular isothermal spheres (the model used in this paper for galaxies), three images at most can be produced, and the faintest one is located in the core of the lensing galaxy, making it very difficult to observe. Our experiments do not have such limitations, but are limited by the number of light rays used. An unlensed source contains 190 light rays, and therefore images with a magnification $\mu < 1/190 = 0.0053$ are unresolved.

5.5.3. Double Images

For each model, we computed the probability P_2 of finding a double image. The results are plotted in Figure 18. There are 43 points in each panel, corresponding to the 43 different cosmological models considered. The values of P_2 are quite high for the reasons explained above. There is a strong trend of P_2 to increase with λ_0 , as the top right panel of Figure 18 shows.

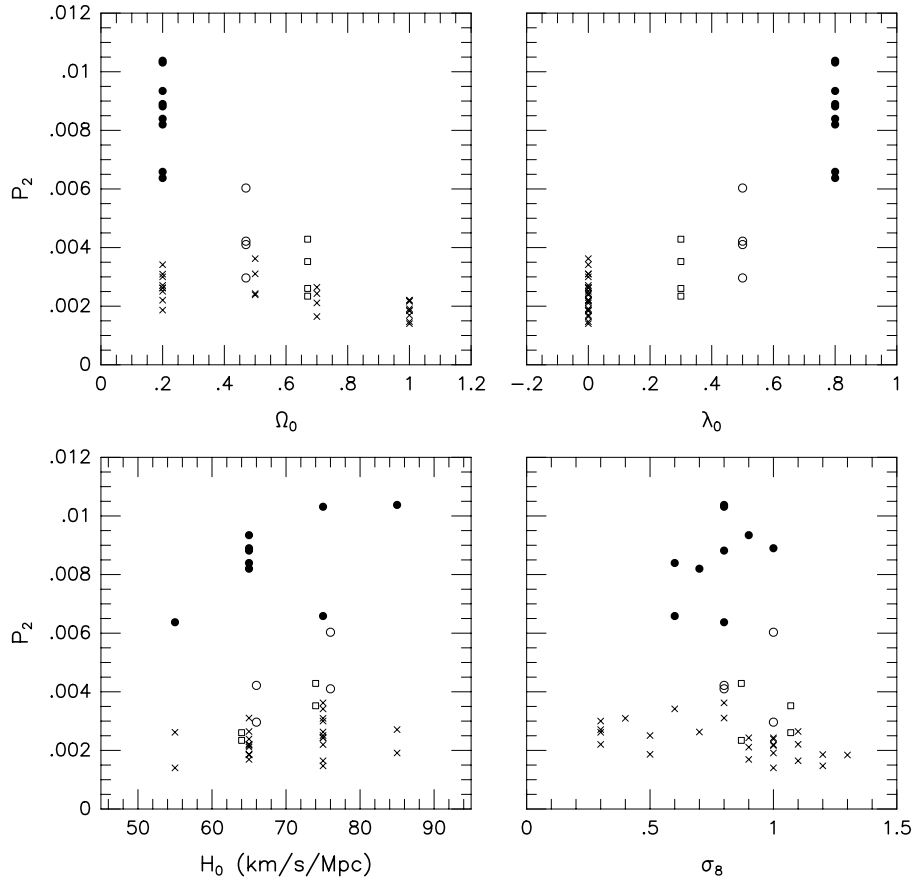


Figure 18: Double-image probability P_2 , versus Ω_0 (top left panel), λ_0 (top right model), H_0 (bottom left panel), and σ_8 (bottom right panel). Each point corresponds to one cosmological model. Symbols indicate the value of the cosmological constant; crosses: $\lambda_0 = 0$; open squares: $\lambda_0 = 0.3$; open circles: $\lambda_0 = 0.5$; filled circles: $\lambda_0 = 0.8$.

In order to study the variations of P_2 with the other parameters *at fixed* λ_0 , we use different symbols to designate the different values of λ_0 . The large scatter in the values of P_2 is clearly caused by the dependence of P_2 upon λ_0 , as the various symbols indicate. On all panels, $\lambda_0 = 0.8$ models (solid circles) are concentrated at the top, while $\lambda_0 = 0$ models (crosses) are concentrated at the bottom. Looking at the crosses in the top left panel, and looking separately at the various symbols in the bottom panels, we find no obvious trend, indicating that P_2 is essentially independent of Ω_0 , H_0 , and σ_8 at fixed λ_0 . These results implies that (i) double images, and multiple images in general, are caused by galaxies and not by the background large-scale structure, (otherwise there would be a strong dependence upon σ_8) and (ii) the strong dependence of P_2 upon λ_0 indicate that the cosmological distances are the dominant effect in multiple imaging.

The most important and interesting property of double images, after their likelihood of occurrence, is the distribution of angular separations between the images. This will be the topic of §5.6 below.

5.5.4. Triple Images

We found 126 cases with triple images, out of a total of 3,137,675 potential sources. With such a small number of cases, we cannot make a quantitative determination of the probability P_3 for occurrence of triple images, and its relationship with the cosmological parameters. Still, we have enough cases to study the general properties of triple images, and to identify trends. It turns out that several of the results found for the double images apply to triple images as well.

We plotted the properties of triple images in Figure 19. The top left panel shows a histogram of the magnification distribution. The magnifications are quite high, usually in the range $\mu = 2 - 7$, with some cases having $\mu > 10$. Triple images are strong lensing events caused by massive galaxies, though the tidal field of the background matter and nearby galaxies might play a key role in determining the shape of the images.

As for the double images, there is a strong trend for triple images to occur in models with a large cosmological constant. We studied 17 models with $\lambda_0 \neq 0$, and found cases of triple images in all of them but one: the model $\Omega_0 = 0.7$, $\lambda_0 = 0.3$, $H_0 = 65 \text{ km s}^{-1} \text{ Mpc}^{-1}$, $\sigma_8 = 0.9$, for which we have performed 64 experiments. We also studied 26 models with $\lambda_0 = 0$, and found cases of triple images in only 13 of them, in spite of the fact that we have performed more experiments for these models than the $\lambda_0 \neq 0$ models. The top right panel of Figure 19 shows the frequency of occurrence of triple images, defined as the number of cases (indicated by numbers) divided by the number of experiments, versus λ_0 . About one fifth of the cases (27 out of 126) were found in models with $\lambda_0 = 0$, but 71% of the experiments (2,699 out of 3,798) were performed with these models. The trend is clear: the frequency of triple images increases sharply with λ_0 . As for the double images, this indicate that the cosmological distances are the dominant effect.

The bottom left panel of Figure 19 is the scatter plot of the brightness ratios B_2/B_3 and B_1/B_2 , where B_1 , B_2 , and B_3 are the brightnesses of the brightest, intermediate, and faintest images, respectively. The dashed line corresponds to $B_2/B_3 = B_1/B_2$. The brightness ratios can be very large, up to ~ 100 , and for this reason we decided to use logarithmic scales. Triple images located above the dashed line have $B_2/B_3 > B_1/B_2$, and are composed of “two bright images and a faint one,” while triple images located below the dashed line have $B_2/B_3 < B_1/B_2$, and are composed of “one bright image and two faint ones.” These latter cases outnumber the former ones 2 to 1. This shows that individual galaxies are not solely responsible for the formation of triple images, since a galaxy modeled as a nonsingular isothermal sphere could only produce a triple image composed of two bright images and one faint, possibly unresolved image. Tidal perturbation by nearby galaxies and by the background matter, and lensing by several galaxies, must play an important role.

The bottom right panel of Figure 19 is a scatter plot of the minimum angular separation s_{\min} and maximum angular separation s_{\max} between the images, in arc seconds. We can identify three specific limiting cases: (i) In the *circular limit*, defined by $s_{\min} = s_{\max}$ (top dashed line), the three images form a circular pattern, as in Figure 13f. (ii) In the *linear limit*, defined by $s_{\min} = s_{\max}/2$ (bottom dashed line), the three images form a linear pattern, with the two outside images equidistant from the central one. These are the kind of triple images that a nonsingular isothermal sphere would produce. (iii) In the *hierarchical limit*, defined by $s_{\min} \ll s_{\max}$ (horizontal axis), two images are very close to each other, with the third image located much farther. These would invariably correspond to cases of one bright image and two faint ones, since the two images located near each other would have to be faint in order not to overlap. As Figure 19

shows, none of these limits seems to be preferred. The scatter is large, and the only noticeable thing is that the strong hierarchical limit does not seem to occur very often, as very few points are located near the horizontal axis.

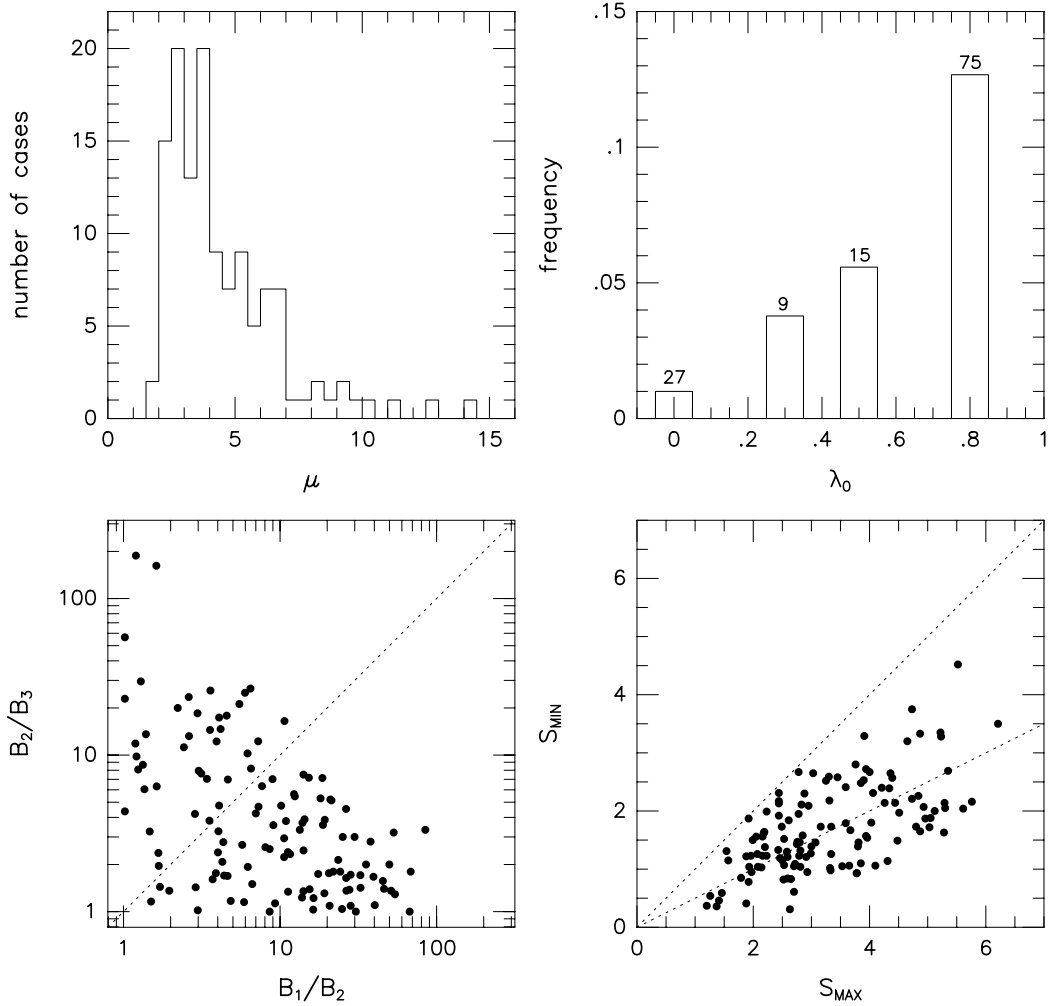


Figure 19: Properties of the triple images. Top left panel: Histogram of the magnification μ . Top right panel: Frequency of occurrence of triple images versus λ_0 . The numbers indicate the actual number of cases found. The frequency is that number divided by the number of experiments. Bottom left panel: brightness ratio B_2/B_3 (intermediate to faintest) versus brightness ratio B_1/B_2 (brightest to intermediate). The dashed line corresponds to $B_2/B_3 = B_1/B_2$. Bottom right panel: minimum angular separation S_{\min} versus maximum angular separation S_{\max} . The dashed lines correspond to the “circular limit” $S_{\min} = S_{\max}$ and the “linear limit” $S_{\min} = S_{\max}/2$.

5.5.5. Quadruple Images

Quadruple images are extremely rare. We only found 6 cases, and two of them are plotted in Figure 13. All cases were found in models with $\lambda_0 = 0.8$, reinforcing the trend of multiple images being more frequent in models with large cosmological constant. The magnifications are $\mu = 2.119, 2.910, 4.846, 8.344, 11.222,$ and 14.012 . With 3 cases out of 6 having $\mu > 8$, quadruple images are even stronger lensing events than triple images. According to the odd-number theorem, each of these cases must be at least a quintuple image with one faint, unresolved image. This is most likely the case for the quadruple image shown in Figure 13j.

These images form a circular pattern, and there is probably a fifth, unresolved image in the center. More complex cases, such as the one shown in Figure 13i, could very well have more than 5 images.

5.6. The Distribution of Image Separations

5.6.1. Histograms of the Image Separations

For each case with multiple images found in the experiments, we computed the angular separation between the images. The center of each image is computed using equation (28), and separations are computed between image centers. Figures 20 and 21 show histograms of the angular separations in arc seconds, for all models. All histograms are plotted on the same scale to facilitate comparison. On each panel, we have indicated the total number N_2 of double images found. This number varies among the different models, first because some models are more likely to produce multiple images than others, and second because the number of experiments performed was not the same for all models. Models with $N_2 < 200$ tend to have very noisy distributions, and many more experiments would be required in order to determine the precise shape of these distributions. Still, several trends are apparent. We are considering sources with an angular diameter of $1''$. Since one image at least must be brighter than the unlensed source would be (SEF, p. 172, Theorem 2), the smallest possible image separation is $0.5''$ corresponding to a double image like the one shown in Figure 13c. Most histograms in Figures 20 and 21 show a distribution that rises sharply from $0.5''$ to $1''$, and then drops slowly at larger separations, with a high-tail that extends to separations of order $4'' - 6''$.

As in the case of the double-image probability P_2 discussed in §5.5.3 above, we find no obvious correlation between the shape of the histograms and the value of σ_8 . This again indicates that double images are caused primarily by direct interaction between the beam and individual galaxies, and not by the large-scale structure. There is, however, a relationship between the largest angular separations and the value of λ_0 . For models with $\lambda_0 = 0$, the high-tail of the distribution function rarely extends beyond $4''$, while for $\lambda_0 = 0.8$ models, the high-tail often extends to separations of $6''$. As for the probability P_2 , the shape of the high-tail depends strongly upon the cosmological distances. Increasing these distances results in higher image separations for a given lensing galaxy. This affects the magnification distribution, by extending the high-tail to higher separation, and also the probability P_2 , by “separating” images that otherwise would have overlapped and been detected as a single image. Fukugita et al. (1990) found that the image separations were independent of the cosmological constant, but only considered the rms value $\langle s^2 \rangle^{1/2}$ of the separation, and not the actual distributions. Since cases with large separations are rare, the details of the high-tail can hardly affect the rms value, and therefore these results are not in contradiction.

In several histograms, especially the ones for $\lambda_0 > 0$ models, we see a secondary peak at large separation. Consider for instance the model $\Omega_0 = 0.2$, $\lambda_0 = 0.8$, $H_0 = 65 \text{ km s}^{-1} \text{ Mpc}^{-1}$, $\sigma_8 = 0.8$, which is indicated by an asterisk in Figure 20. There are no double images with separations between $4.00''$ and $4.75''$, but there are several images with separations larger than $4.75''$. This might seem like a very small effect that could be dismissed as a statistical fluctuation, but this feature is found in many histograms, suggesting that it could actually be real. This could possibly result from a coupling between galaxies and large-scale structure. Galaxies are predominantly responsible for multiple imaging. But most galaxies are located inside clusters, where the density of background matter is high. This background matter might amplify the lensing effect of the galaxy, resulting in a peak at high separation angles. This issue requires more investigation.

5.6.2. A Synthetic Angular Separation Distribution

To gain more insight into the origin and properties of the angular separation distributions shown in Figures 20 and 21, we will now synthesize an angular separation distribution using a simple analytical model. We consider the $\Omega_0 = 0.2$, $\lambda_0 = 0.8$, $H_0 = 65 \text{ km s}^{-1} \text{ Mpc}^{-1}$, $\sigma_8 = 0.8$ model, and make the following assumptions: (1) Lensing is entirely caused by galaxies; we ignore the lensing by the background matter. (2) Each galaxy acts as if it was alone; we ignore the tidal effects of nearby galaxies, and the possibility of lensing events involving several galaxies. With these assumptions, the problem is reduced to studying lensing by isolated, nonsingular isothermal spheres. A problem of such importance has generated a great deal of interest in the past, and several analytical results have been derived (Dyer 1984; Hinshaw & Krauss

1987; Blandford & Kochanek 1987; Kochanek & Blandford 1987) which we can now apply to our model. We use the notation of SEF, §12.2.3.

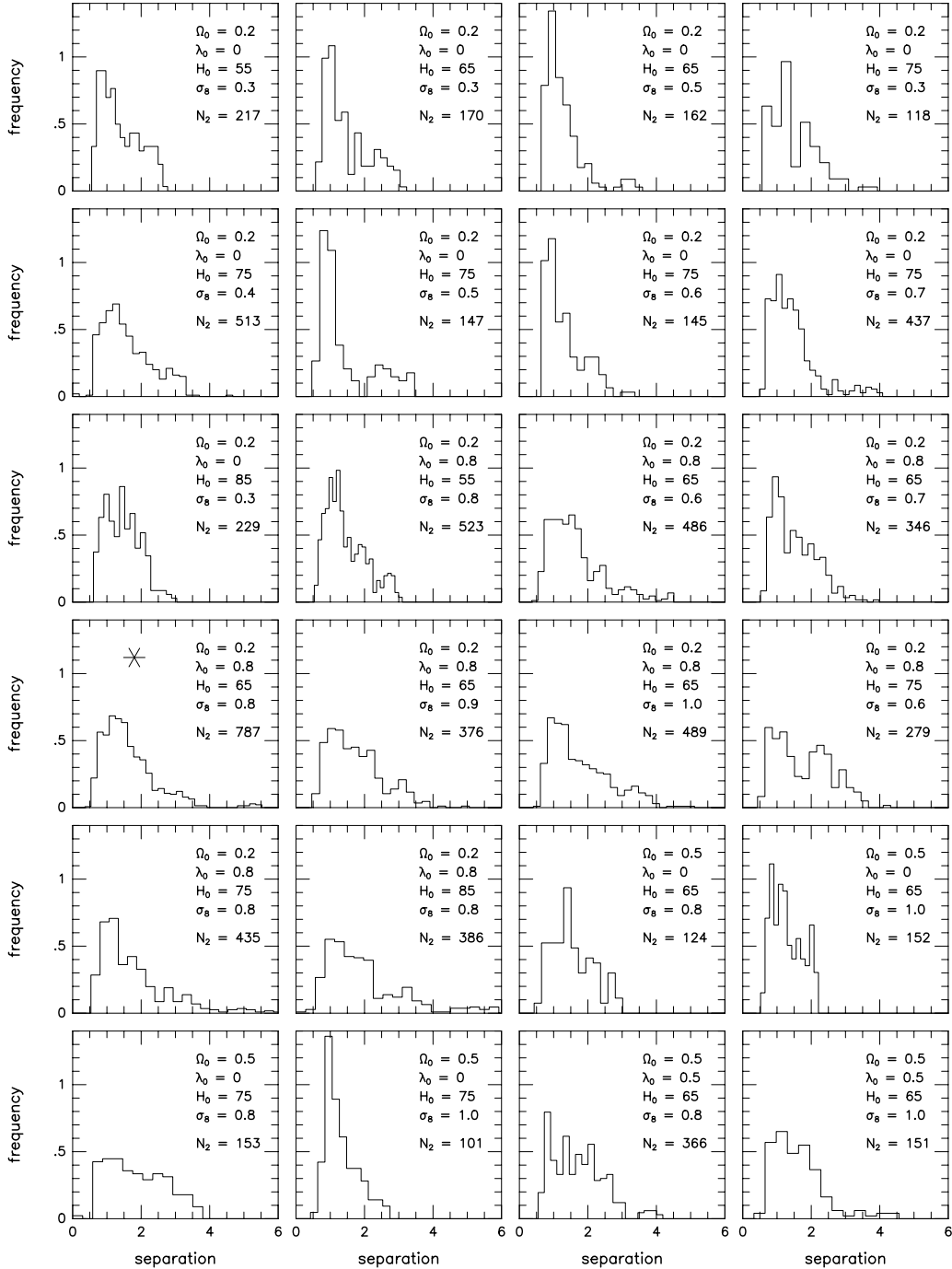


Figure 20: Histograms of the distribution of image separations in arc seconds. The value of the cosmological parameters and the number of double images are indicated in each panel (with H_0 in units of $\text{km s}^{-1} \text{Mpc}^{-1}$). The large asterisk indicates the distribution which is replotted in the bottom panel of Fig. 22.

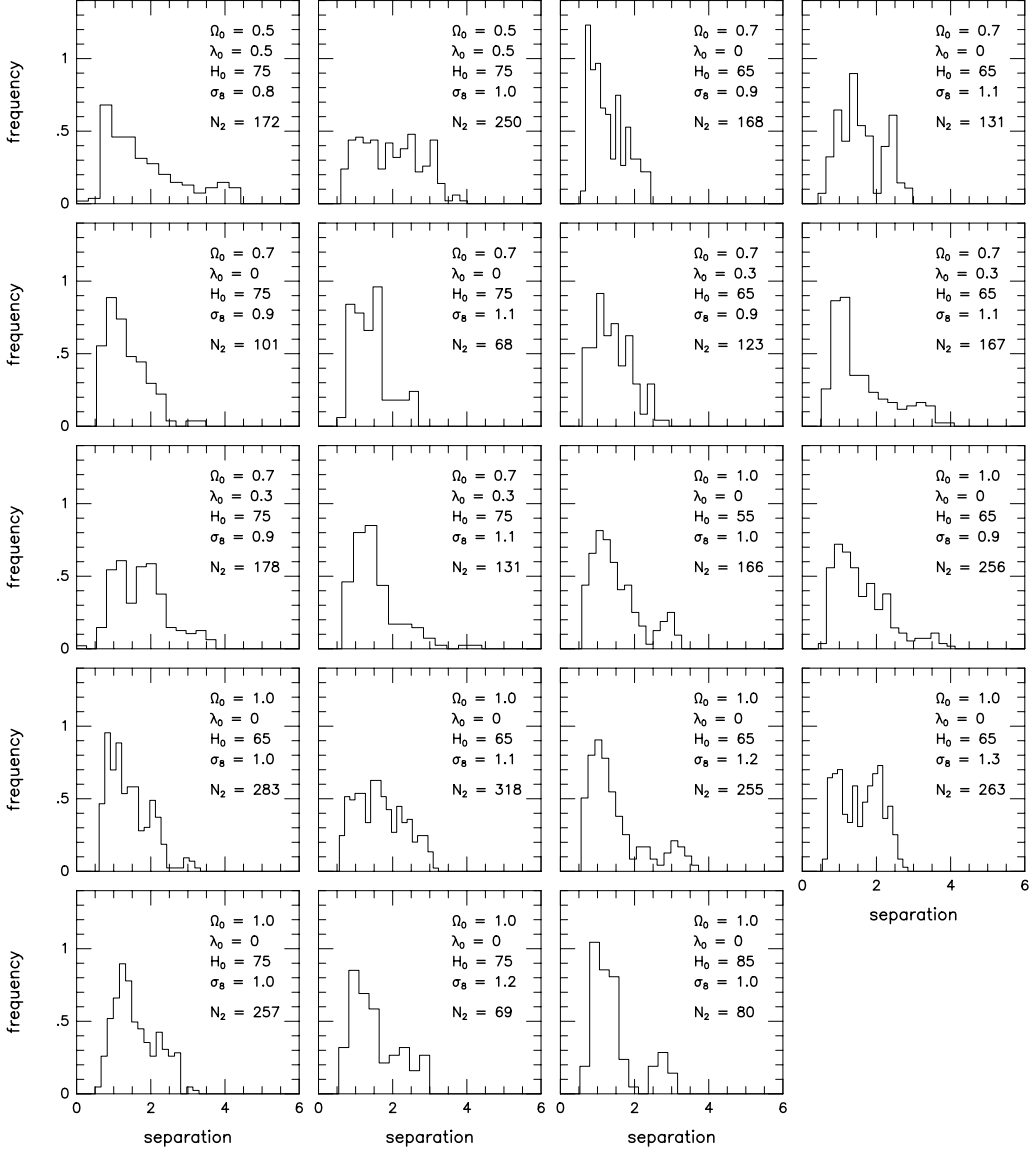


Figure 21: Same as Fig. 20, for different cosmological models.

For each galaxy, we introduce a length scale ξ_0 , defined by

$$\xi_0 = 2\pi \left(\frac{v}{c}\right)^2 \frac{D_L D_{LS}}{D_S} \quad (31)$$

(SEF, eq. [8.34a], with $v = \sqrt{2}\sigma_v$), where v is the circular velocity given by equation (8). We now define the scaled quantities $x_c \equiv r_c/\xi_0$ and $y = \eta/\xi_0$, where r_c is the core radius given by equation (6), and η is the distance between the source and the optical axis going through the observer and the center of the lens. We also define, for $x_c < 1$, a critical radius $y_r \equiv (1 - x_c^{2/3})^{3/2}$. The nonsingular isothermal sphere has the following properties (SEF, §12.2.3): (1) If $x_c \geq 1$, the source will have only one image. (2) If $x_c < 1$ the source will have one image if $y \geq y_r$, and 3 images if $y < y_r$. Hence, each lens which satisfies the condition $x_c < 1$ has a cross section for multiple imaging equal to πy_r^2 .

In our analytical model, we consider as potential lenses all the galaxies located between the source and the observer. 12% of the galaxies, located mostly at redshifts $z < 0.1$ or $z > 2$, are rejected as unable to

produce multiple images, having scaled core radii $x_c > 1$. The top panel of Figure 22 shows the distribution x_c for the remaining galaxies. The distribution is bimodal, with most early type galaxies (ellipticals and S0's) having $x_c < 0.05$, and most spiral galaxies having $0.2 < x_c < 1$. In our model, spiral galaxies have core radii that are typically 10 times larger and circular velocities that are typically twice smaller than early type galaxies, as Table 1 shows. Since $x_c \propto r_c/v^2$, we expect the values of x_c to be typically 40 times smaller for early type galaxies than for spiral galaxies, explaining the bimodal distribution shown in Figure 22. The spread in the distribution within each peak is caused by the dependence of r_c and v upon the luminosity L .

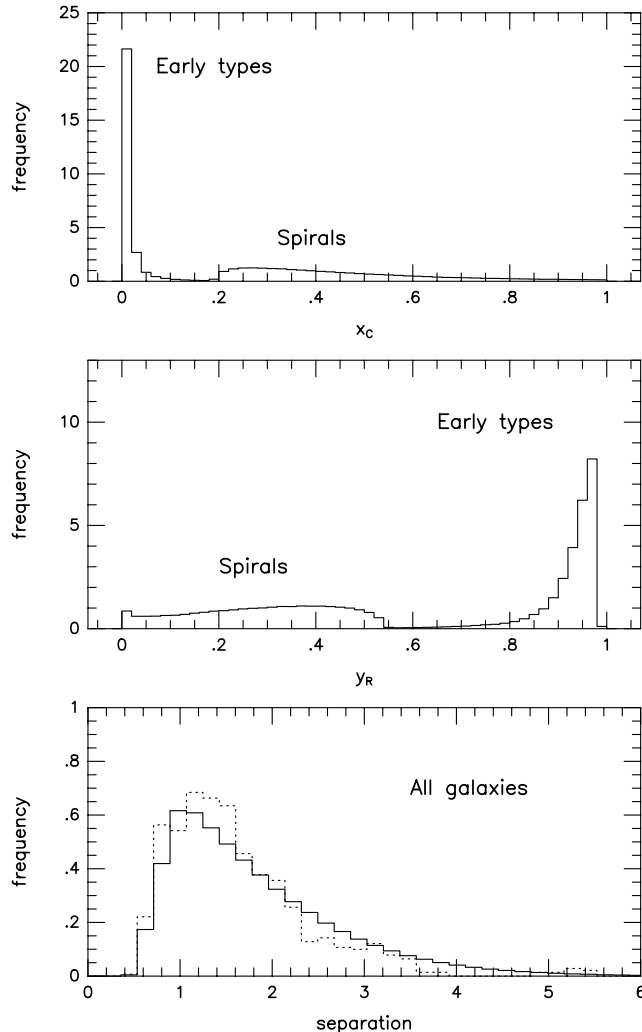


Figure 22: Synthetic angular separation distribution for $\Omega_0 = 0.2$, $\lambda_0 = 0.8$, $H_0 = 65 \text{ km s}^{-1} \text{ Mpc}^{-1}$, $\sigma_8 = 0.8$ model. Top panel: distribution of scaled core radii x_c . Middle panel: distribution of critical radii y_r . Bottom panel: synthetic angular separation distribution (solid line), and actual distribution, taken from the thirteenth panel of Fig. 20 (dotted line). See text for details.

The second panel of Figure 22 shows the distribution of critical radii. Small values of x_c lead to large values of y_r , and vice versa. Early type galaxies have critical radii concentrated near the maximum possible value $y_r = 1$,¹⁶ while spiral galaxies have $y_r < 0.55$. Hence the cross section for multiple imaging is dominated by early type galaxies.

If a galaxy modeled as a nonsingular isothermal sphere produces multiple images (that is, 3 images), the angular separation s between the two outermost images depends upon the source position y , and has a

¹⁶ $y_r = 1$ would require $r_c = 0$, that is, a *singular* isothermal sphere

maximum value given by

$$s_{\max} = \frac{2\xi_0}{D_L}(1 - x_c^2)^{1/2}. \quad (32)$$

Hinshaw & Krauss (1987), and Cheng & Krauss (1999) showed that the dependence of s on y is weak. Following the suggestion made by SEF (p. 396), we will assume that whenever multiple images occur, the image separation is of order $s \sim s_{\max}$. We can then compute the distribution of image separations directly from the distribution of scaled core radii x_c . In doing so, we found out that many separations are significantly smaller than the source size, in which case the images strongly overlap and would be observed as one single image. To build a realistic distribution, we must impose limits on the smallest possible image separation that allows individual images to be resolved. We assume that sources have an angular diameter of $1''$. The smallest possible image separation is therefore $0.5''$, corresponding to an image configuration such as the one shown in Figure 13c. However, with such small image separations, the images will often overlap (Fig. 13c is a particular, “lucky” case). We assume that at separations $s < 0.5''$ the individual images can never be resolved, that at separations $s > 1''$ they can always be resolved, and that at separations $0.5'' < s < 1''$ they can sometimes be resolved, with a probability that varies linearly from 0 to 1 between $s = 0.5''$ and $s = 1''$. The requirement that s must exceed $0.5''$ in order to possibly create resolvable multiple images eliminates as potential lenses about half of the early time galaxies, and 97% of the spiral galaxies. Hence, early types galaxies are much more likely to produce resolved multiple images than spiral galaxies. Not only the early type galaxies capable of producing resolvable multiple images outnumber the spiral galaxies 20 to 1, but their cross sections for multiple imaging are larger, as the second panel of Figure 22 shows. Notice, however, that both the numerical simulations and the analytical model treat galaxies as isothermal spheres. Blain, Möller, & Maller (1999) have shown that the presence of a galactic disc can significantly increase the cross section for multiple imaging. Hence, our simulations and analytical model probably underestimate the contribution of spiral galaxies to multiple imaging.

We computed the distribution of angular separations, using the above criterion for “resolvability.” We also gave to each galaxy a weight $w = y_r^2$ to take the effect of cross section into account. The resulting distribution is shown in the bottom panel of Figure 22, by the solid line. For comparison, we plotted the actual distribution (dotted line) for this particular model, taken directly from the thirteenth panel of Figure 20 (indicated by an asterisk). The agreement is quite remarkable. The synthetic distribution reproduces the main features of the actual distribution: a sharp rise at separations $s < 1''$, and a slow decline at separations $s > 1''$. The analytical model underpredicts the number of cases with separations $s \sim 1'' - 1.6''$, and overpredicts the number of cases with separations $s > 2.4''$. This is probably a consequence of ignoring the presence of the background matter.

For the particular cosmological model considered in this section, we found 787 cases with double image. Because this number is quite high, we are confident that the distribution of image separations is fairly well determined by the experiments. Hence, the bottom panel of Figure 22 serves to validate the analytical model. Armed with the knowledge that the analytical model can reproduce, to a reasonable accuracy, the actual distribution of separations, we intend to perform a much more detailed study of these distributions and their relationship to the cosmological parameters, based on the analytical model instead of ray tracing experiments. This study will be presented in a forthcoming paper (Martel, Premadi, & Matzner 2001).

5.7. Einstein Rings

Einstein rings are very common in our experiments, but most of them are rather unspectacular: The image contains a few hundred rays, and the hole is made of a small number of “missing” rays, often less than 10. Such holes have an angular diameter D_{hole} of order $0.1''$ or less, and it is doubtful that observations could possibly resolve such small holes. Only the most massive galaxies can produce spectacular rings with hole angular diameters of order $1''$, such as the one shown in Figure 13d, but since only a small fraction of galaxies are very massive, such spectacular rings are quite rare.

We need to decide where to draw the line between holes that are too small to be resolved, and holes that are not. This is obviously a very subjective decision, especially since the possibility of resolving small holes depends upon the details of observation and instrumentation. We decided, quite arbitrarily, to exclude from this study rings with a hole diameter $D_{\text{hole}} < 0.64''$. Because this choice is arbitrary, we cannot derive precise statistics of the occurrence of rings and its dependence upon the cosmological parameters. We

can only describe the intrinsic properties of the rings, and express their relationship with the cosmological parameters in terms of general trends.

The properties of the Einstein rings are summarized in Figure 23. The top left panel shows a histogram of the number of rings found versus their magnification μ . This shows that rings are usually high-magnification events. The histogram peaks at a magnification $\mu \sim 5$, and then drops slowly with magnification. Several rings have a magnification $\mu > 10$, and the largest magnification we encountered was $\mu = 24.097$ (it is the double ring shown in Fig. 13m). This justifies our use of the term “spectacular” to designate such rings.

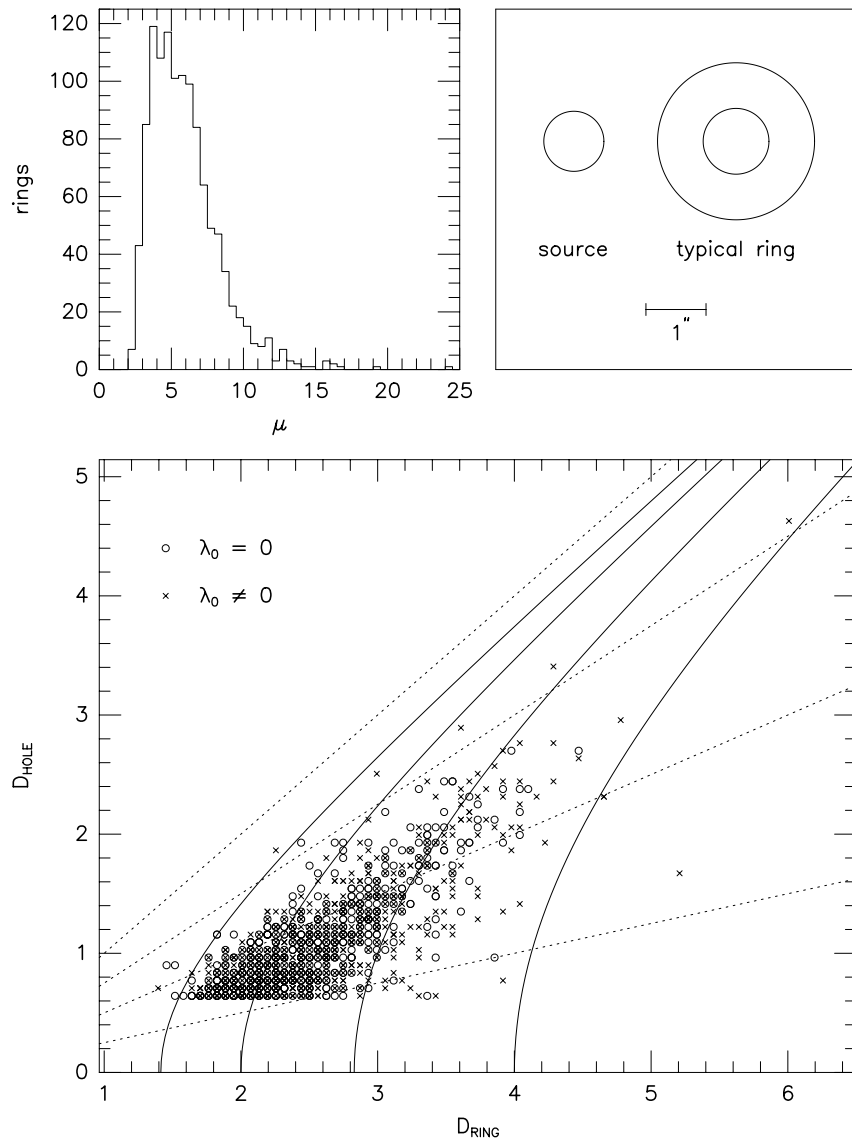


Figure 23: Properties of the rings. Top left panel: histogram of the number of rings versus magnification μ . Top right panel: schematic plot showing the image of an unlensed source and a “typical ring,” obtained by averaging the properties of all the rings found in the simulations. The horizontal bar indicates 1 arc second. Bottom panel: scatter diagram of the hole diameter D_{hole} versus ring diameter D_{ring} measured in arc second. The different symbols indicate models with and without a cosmological constant. The solid curves, from top to bottom, correspond to magnifications $\mu = 2, 4, 8, \text{ and } 16$. The dotted lines, from left to right, correspond to thickness parameters $T_{\text{ring}} = 0.00, 0.25, 0.50, \text{ and } 0.75$.

The top right panel of Figure 23 shows a “typical” ring, obtained by averaging the ring diameters D_{ring} (the outer diameter of the images) and the hole diameters D_{hole} over all rings found in all experiments. The average hole diameter is $\langle D_{\text{hole}} \rangle = 1.09''$, slightly larger than an unlensed source. The average ring diameter is $\langle D_{\text{ring}} \rangle = 2.62''$.

In the bottom panel of Figure 23, we plot the distribution of ring diameters and hole diameters in arc seconds. The solid curves are contours of constant magnification, from left to right: $\mu = 2, 4, 8$, and 16 . Most rings have magnifications between $\mu = 4$ and $\mu = 8$ as we saw also in the histogram. The circles and crosses indicate models with $\lambda_0 = 0$ and $\lambda_0 \neq 0$, respectively. Rings with $\mu < 8$ are found in comparable numbers in both cases, but rings with $\mu > 8$ are found predominantly in models with $\lambda_0 \neq 0$, and particularly in models with $\lambda_0 = 0.8$. This is the most important trend we found. The largest magnifications we have encountered, $\mu = 19.446$ and $\mu = 24.097$, were for models with $\lambda_0 = 0.8$. We also found a weaker trend: μ tends to increase with H_0 . The dashed lines are, from top to bottom, lines of constant thickness parameter $T_{\text{ring}} = 0.00, 0.25, 0.50$, and 0.75 , where the thickness parameter is defined by

$$T_{\text{ring}} \equiv \frac{D_{\text{ring}} - D_{\text{hole}}}{D_{\text{ring}}}. \quad (33)$$

An infinitely thin ring has $D_{\text{hole}} = D_{\text{ring}}$ and $T_{\text{ring}} = 0$; an infinitely thick ring has $D_{\text{hole}} = 0$ and $T_{\text{ring}} = 1$. Figure 23 shows that most rings are quite thick, having T_{ring} in the range $0.5 - 0.75$. The typical ring shown in the top right panel has a thickness parameter $T_{\text{ring}} = 0.58$.

6. DISCUSSION

The algorithms used for generating the density structures in the universe and for computing the trajectories of light rays are based on a certain number of approximations. In this section, we review these various approximations, and their possible effect on the results.

The #1 approximation of any multiple lens-plane algorithm is that a continuous distribution of matter can be approximated by a finite number of lens planes, and that the results converge if the number of planes is sufficiently high. This issue was investigated by Lee & Paczynski (1990), and more recently by Martel et al. (2000). This latter paper showed that for sources located at redshift $z = 3$, 14 lens planes are sufficient to achieve convergence. In this paper, we used between 26 and 69 planes, depending on the model. Hence, the convergence of our multiple lens-plane algorithm is not an issue.

Our algorithm for locating galaxies inside dense regions, which is described in detail in Paper I, ignores the existence of small-scale correlations, which lead to galaxy pairs such as the Local Group. However, as Figure 10 (bottom panel) shows, pairs of nearby galaxies are actually quite common in our simulations. Most of these pairs are not real physical pairs, being made of galaxies at different distances seen in projection, but this does not matter since only the projected surface density enters in the lens equation. The projected distributions of galaxies would hardly look any different if pairs were explicitly included in the algorithm.

The relation given by equation (8), relating the circular velocity to the luminosity, might break down in the limit of small luminosities. This would not affect the magnification and shear distributions, which are determined primarily by the background matter, but it could affect the distribution of image separations. However, using the equations given in §5.6.2, we can easily show that the high-luminosity galaxies have larger cross sections for multiple imaging, and produce larger separations. With a Schechter luminosity function, low-luminosity galaxies are exponentially more abundant, but this does not affect the results because these galaxies produce separations that are much too small to be resolved. As we indicate in §5.6.2, imposing a minimum separation of $0.5''$ “eliminates” half of the early type galaxies and 97% of the spiral ones, and most of these galaxies are low-luminosity.

Galaxies evolve. Not only their number density changes as a result of merging, but their individual density profiles might change also. We decided to ignore these effects in the current paper. Our method for locating galaxies in the computational volume is only approximate, and one might question the relevance of adding detailed modeling of the merging history and galaxy evolution, considering the uncertainties already present in the algorithm. We believe that our neglect of galaxy evolution and merging does not affect our results significantly. First, the weak lensing (magnification and shear) is unaffected by the galaxies. As for the strong lensing, the effect can be important. However, one critical point is that this paper presents a

comparative study of cosmological models. Some of the lensing properties might change if the algorithm is modified. But these changes would not necessarily affect the trends seen in the variations of these properties with the cosmological parameters. To give a specific example: consider the double image probability P_2 plotted in Figure 18. Would the values of P_2 be different if we had used different models galaxies? Most certainly. Would the trends revealed by Figure 18 (P_2 increasing strongly with λ_0 , with no dependence on Ω_0 , H_0 and σ_8) be different? Very unlikely. The focus of this paper was to determine the relationship between the lensing properties and the cosmological parameters. We intend to present a study of the effect of galaxy merging, and of considering various radial density profiles of galaxies, in a forthcoming paper. The focus of that paper will be different, and we will certainly not consider 43 different cosmological models.

We superpose on top of each galaxy a “hole” of negative density to represent the matter that has been removed from the intergalactic medium by the galaxy formation process (Paper I). This is certainly the most uncertain part of our algorithm. This uncertainty simply reflects our lack of understanding of the galaxy formation process. At large scales, the density structures are dominated by the distribution of background matter, and the formation of these structures in CDM universes is well understood and accurately simulated by the P³M algorithm. At small scale, the density structures are dominated by galactic halos, and we represent these halos using analytical models that are in good agreement with observations, at least at low redshifts. It is the intermediate scale, immediately above the galactic scale, which is poorly understood. Galaxies must clearly remove matter from the intergalactic medium when they form, but the effect of this removal on the density structure of the intergalactic medium around galaxies is not known. Yet, it cannot be ignored. Adding galaxies to the system using a Monte-Carlo method increases the total mass of the system, and therefore the mass of the background matter must be reduced somehow in order to conserve mass. By superposing a hole on top of each galaxy, we assume that when a galaxy forms, the mass that accumulates in that galaxy comes from its vicinity. This is highly uncertain. Fortunately, the effect of the holes on the lensing properties of galaxies is small. When the beam hits a galaxy, it encounters 3 different density structures: the galaxy itself, the hole superposed on top of the galaxy, and the background matter. Of all these three components, the hole is by far the least important one. The (negative) mass of the hole is equal to the mass of the galaxy, which is much smaller than the mass of the nearby background matter, even for models with $\Omega_0 = 0.2$. Furthermore, the holes are “spread” over radii much larger than the galaxies themselves. These holes should be seen as a small correction to the density of the background, to account for the removal of matter by the galaxy formation process. Notice also that according to the recent paper by Cheng & Krauss (1999), the effect of the background matter on the image separation caused by galaxies is at most 10%, and the presence of the hole introduces only a small correction to this value.

We assume throughout this paper that sources have an angular diameter of 1". To test the effect of the source size on the results, we selected a particular model, $\Omega_0 = 0.2$, $\lambda_0 = 0.8$, $H_0 = 65 \text{ km s}^{-1} \text{ Mpc}^{-1}$, $\sigma_8 = 0.8$, and performed an additional 101 experiments using a smaller beam, $10.95'' \times 10.95''$ instead of $21.9'' \times 21.9''$. With the same number of cells in the beam, this amounts to considering sources of angular diameter 0.5". We found that the magnification distribution $P(\mu)$ is independent of the source size, the distributions for 1" sources and 0.5" sources being nearly identical. However, the image multiplicities are reduced. From $(P_2, P_3, P_4) = (0.00882, 0.00009, 0.00001)$ for 1" sources, they dropped to $(P_2, P_3, P_4) = (0.00616, 0.00006, 0.00000)$ for 0.5" sources. This was expected, since a smaller source does not sample as well the inhomogeneities in the density structure which are responsible for lensing.

7. SUMMARY AND CONCLUSION

We have studied the propagation of light in inhomogeneous universes, for 43 different *COBE*-normalized CDM models with various combinations of Ω_0 , λ_0 , H_0 , and σ_8 . We have performed a total of 3,798 numerical experiments, using a multiple lens-plane algorithm that enabled us to study the properties of weak and strong lensing simultaneously. Each experiments consisted of propagating a square beam of angular size $21.9'' \times 21.9''$, composed of 341×341 light rays, from the observer to a source plane located at redshift $z = 3$. Our main results are the following:

(1) At fixed Ω_0 , λ_0 , and H_0 , the magnification distribution depends upon σ_8 . As σ_8 increases, the low-tail of the magnification distribution shifts toward lower magnifications, because light rays are more likely to propagate through mostly underdense regions. The high-tail of the magnification distribution is

hardly affected. This result indicates that it is the background matter, and not galaxies, that are primarily responsible for the magnification of sources.

(2) At fixed Ω_0 , λ_0 , and σ_8 , the magnification distribution becomes narrower as H_0 increases, reflecting the fact that cosmological distances become shorter. This trend is rather weak, because the distance effect is partly compensated by the fact that the mean background density increases with H_0 .

(3) At fixed H_0 and σ_8 , the low-tail of the magnification distribution shifts to lower values (that is, larger demagnification) as Ω_0 increases for $\lambda_0 = 0$ models, and shifts to higher values as Ω_0 increases for $\Omega_0 + \lambda_0 = 1$ models. In the case $\lambda_0 = 0$, the dependence of the mean background density upon Ω_0 dominates over the respective dependences of the cosmological distances and large-scale structure upon Ω_0 . In the case $\Omega_0 + \lambda_0 = 1$, the dominant effect is the dependence of the cosmological distances upon λ_0 .

(4) At fixed Ω_0 , H_0 , and σ_8 , the magnification distribution becomes wider (that is, stronger lensing) as λ_0 increases, because of the increase in the cosmological distances. The effect is particularly large for models with $\lambda_0 = 0.8$.

(5) The magnification probability P_m is almost independent of σ_8 , for any combination of Ω_0 , λ_0 , and H_0 , indicating that P_m does not depend strongly on the amount of large-scale structure. Our interpretation is that the beam travels through several underdense and overdense regions whose effects mostly cancel out. Increasing σ_8 makes the underdense regions more underdense and overdense regions more overdense, but their effects still mostly cancel out. The only trend we found is that P_m increases with Ω_0 at fixed λ_0 , H_0 , and σ_8 . This suggests that P_m depends primarily on the mean background density.

(6) The shear distribution has essentially the same dependences upon the cosmological parameters as the magnification distribution. At fixed Ω_0 , λ_0 , and H_0 , the shear distribution becomes wider with increasing σ_8 . At fixed Ω_0 , λ_0 , and σ_8 , the shear distribution is very insensitive to the value of H_0 . At fixed H_0 and σ_8 , the shear distribution becomes wider with increasing Ω_0 for $\lambda_0 = 0$ models, and narrower with increasing Ω_0 (and correspondingly decreasing λ_0) for $\Omega_0 + \lambda_0 = 1$ models. At fixed Ω_0 , H_0 , and σ_8 , the shear distribution becomes wider as λ_0 increases.

(7) The similarities found between the properties of the magnification distribution and shear distribution suggests that both phenomena have the same origin: weak lensing. The dependence of the magnification distribution upon σ_8 is a clear indication that the large-scale structure in the background matter, and not individual galaxies, are responsible for determining this distribution. This occurs because galaxies cover only a small fraction of each lens plane, and are not too likely to be hit by the beam. This argument does not apply to the shear distribution, however, since shear is not caused by the matter being directly hit by the beam, but rather by the distant matter. In this case, the absence of significant contribution from galaxies originate from their small mass (at most 24% of the total mass is in galaxies), and by the presence, in the algorithm, of a compensating underdensity on top of each galaxy to account for the mass removed from the background matter during the galaxy formation process. The strong dependence of the magnification and shear distribution upon λ_0 indicate that while the large-scale structure is responsible for these effects, the magnitude of these effects depends strongly upon the cosmological distances.

(8) The double-image probability P_2 increases strongly with λ_0 . We found no clear dependence upon Ω_0 , H_0 , and σ_8 . The absence of dependence upon σ_8 indicates that individual galaxies, and not the background matter are responsible for forming double images, which constitute examples of strong lensing. The strong dependence upon λ_0 indicates that, again, the dominant effect is the cosmological distances.

(9) The distribution of image separations has properties similar to the probability P_2 : a strong dependence upon λ_0 and no dependence upon σ_8 . The distribution rises sharply from $0.5''$, half the angular diameter of the source, to $1''$, and then drops slowly, down to separations of order $4''$ for $\lambda_0 = 0$ models and $6''$ for $\lambda_0 = 0.8$ models. In many cases, we also found a small, secondary peak in the distribution at separations of order $5''$.

(10) Using an analytical model, which assumes that multiple images are entirely caused by galaxies, we have generated a synthetic distribution of image separations for one of the model. This synthetic distribution reproduces the actual distribution obtained from the simulations remarkably well, indicating that the assumption of galaxies being responsible for generating multiple images is correct. The only discrepancies are at separations of $1'' - 1.6''$, where the synthetic distribution is too low, and at separation larger than $2.4''$, where the synthetic distribution does not drop fast enough. These discrepancies probably result from the presence of the background matter, which is ignored in the analytical model.

(11) We only found 126 cases of triple images and 6 cases of quadruple images. With such small numbers, we cannot do any precise determination of the probabilities P_3 and P_4 , but we can identify several trends. Triple and quadruple images are strong lensing, high-magnification events caused by galaxies. Their magnification distribution peaks around $\mu = 4$, and the high-tail extends to values larger than $\mu = 10$. These cases are predominantly found in $\lambda_0 > 0$ models, indicating again that the effect of the cosmological distances dominates. Triple images come out in a variety of pattern, including circular and linear patterns. About 2/3 of the triple images are made of one bright image and two faint ones.

(12) It is difficult to determine precise statistics for the occurrence of Einstein rings. Rings are very common, but we rejected most of them because the “hole” was very small. We only included in the analysis rings with hole diameters larger than $0.64''$. Rings are the most extreme cases of strong lensing found in our experiments. Most rings have magnifications in the range $\mu = 4 - 8$, and the magnification distribution extends to $\mu = 25$. The brightest image found in any given experiment is almost always a ring. Rings are usually quite thick, with a thickness comparable to the angular size of the source. Rings are found both in $\lambda_0 = 0$ models and $\lambda_0 > 0$ models, but bright rings, with $\mu > 8$, are found predominantly in $\lambda_0 > 0$ models.

We can summarize these results as follows: (1) The cosmological distances play a critical role in nearly every aspect of gravitational lensing, both weak and strong. Consequently, the properties of gravitational lenses depend much more strongly upon the cosmological constant λ_0 than any other cosmological parameter. (2) Magnification and shear are examples of weak lensing caused primarily by the distribution of background matter, with negligible contribution from galaxies. Consequently, these effects are sensitive to the value of the rms density fluctuation σ_8 . (3) Multiple images and rings are examples of strong lensing, caused by direct interaction with galaxies, with at most a small contribution from the background matter. Consequently, the properties of multiple images are independent of σ_8 . They are determined by the cosmological distances, which depend primarily upon λ_0 , and by the details of the galactic models, which are usually independent of the cosmological parameters. Therefore, observations of weak lensing can be used to determine the cosmological constant and the *unbiased* density structure of the universe (that is, without having to assume some biasing factor between luminous and dark matter), while observations of strong lensing can be used to determine the cosmological constant and the internal structure of galaxies and clusters. (4) The dependences upon H_0 and Ω_0 are not as simple, because varying these parameters affects gravitational lensing in several ways that often partly cancel each other. For instance, the small dependence of the magnification and shear distribution upon H_0 results from the competing effects of increasing cosmological distance while reducing the mean background density. Determining λ_0 and σ_8 from observations seems much more promising than determining Ω_0 and H_0 .

Our experiments consider only sources located at redshift $z = 3$, in which case most of the matter responsible for lensing is located at redshifts $z \sim 1$. This is not an important limitation of our study. As Figure 5 shows, the angular diameter distances vary only weakly with redshift in the limit $z > 1$. Hence, our conclusions remain valid for sources located at larger redshifts.

In conclusion, our study shows that it is difficult to single out the effect of each particular cosmological parameter. This supports the idea of conducting this simultaneous cosmological parameter survey.

This work benefited from stimulating discussions with Andrew Barber, Christopher Fluke, Takashi Hamana, Peter Schneider, and an anonymous referee. We are pleased to acknowledge the support of NASA Grant NAG5-2785, NSF Grants PHY93 10083 and ASC 9504046, Grant 3658-0624-1999 from the Texas Advanced Research Program, the University of Texas High Performance Computing Facility through the office of the vice president for research. PP gratefully acknowledges the Postdoctoral Fellowship from the Japan Society for the Promotion of Science and the hospitalities of the Astronomical Institute of Tohoku University, and the Centre for Relativity of the University of Texas at Austin.

REFERENCES

- Albrecht, A., & Steinhardt, P. 1982, Phys.Rev.Lett., 48, 1220
 Asada, H. 1997, ApJ, 485, 460
 Babul, A., & Lee, M. H. 1991, MNRAS, 250, 407
 Bacon, D. J., Refregier, A., & Ellis, R. S. 2000, MNRAS, submitted (astro-ph/0003008)
 Bardeen, J. M., Bond, J. R., Kaiser, N., & Szalay, A. S. 1986, ApJ, 304, 15

Bartelmann, M., & Schneider, P. 1991, *A&A*, 248, 349
 Bartelmann, M., Huss, H., Colberg, J. M., Jenkins, A., & Pearce, F. R. 1998, *A&A*, 330, 1
 Blain, A. W., Möller, O., & Maller, A. H. 1999, *MNRAS*, 303, 432
 Blandford, R. D., & Kochanek, C. S. 1987, *ApJ*, 321, 658
 Blandford, R. D., & Nayaran, R. 1986, *ApJ*, 310, 568
 Bloomfield Torres, L. F., & Waga, I. 1996, *MNRAS*, 279, 712
 Bucher, M., Goldhaber, A. S., & Turok, N. 1995, *Phys.Rev.D*, 52, 3314
 Bunn, E. F., & White, M. 1997, *ApJ*, 480, 6
 Burles, S., & Tytler, D. 1998, *ApJ*, 499, 699
 Charlton, J. C., & Turner, M. S. 1987, *ApJ*, 313, 495
 Cheng, Y.-C. N., & Krauss, L. M. 1999, *ApJ*, 514, 25
 Chiba, M., & Futamase, T. 1999, *Prog.Th.Phys*, 133, 115
 Chiba, M., & Yoshii, Y. 1997, *ApJ*, 489, 485
 Chiba, M., & Yoshii, Y. 1999, *ApJ*, 510, 42
 Cooray, A. R., Quashnock, J. M., & Miller, M. C. 1999, *ApJ*, 511, 562
 Couchman, H. M. P., Barber, A. J., & Thomas, P. A. 1999, *MNRAS*, 308, 180
 Davis, M., Efstathiou, G., Frenk, C. S., & White, S. D. M. 1985, *ApJ*, 292, 371
 Dressler, A. 1980, *ApJ*, 236, 351
 Dyer, C. C. 1984, *ApJ*, 287, 26
 Efstathiou, G., Ellis, R. S., & Peterson, B. A. 1988, *MNRAS*, 232, 431 (EEP)
 Falco, E. E., Kochanek, C. S., & Muñoz, J. A. 1998, *ApJ*, 494, 47
 Falco, E. E., Shapiro, I. I., Moustakas, L. A., & Davis, M. 1997, *ApJ*, 484, 70
 Filippenko, A. V., & Riess, A. G. 1998, *Physics Reports*, 307, 31
 Fluke, C. J., Webster, R. L., & Mortlock, D. J. 1999, *MNRAS*, 306, 567
 Fry, J. N. 1985, *Phys.Lett.B*, 158, 211
 Fukugita, M., Futamase, T., & Kasai, M. 1990, *MNRAS*, 246, 24P
 Fukugita, M., Futamase, T., Kasai, M., & Turner, E. L. 1992, *ApJ*, 393, 3
 Gilliland, R. L., Nugent, P. E., & Phillips, M. M. 1999, *ApJ*, 521, 30
 Guth, A. 1981, *Phys.Rev.D*, 23, 347
 Hamana, T., Martel, H., & Futamase, T. 2000, *ApJ*, 529, 56
 Hinshaw, G., & Krauss, L. M. 1987, *ApJ*, 320, 468
 Hockney, R. W., & Eastwood, J. W. 1981, *Computer Simulation Using Particles* (New York: McGraw-Hill)
 Hu, W., & Sugiyama, N. 1996, *ApJ*, 471, 542
 Im, M., Griffith, R. E., & Ratnatunga, K. U. 1997, *ApJ*, 475, 457
 Jaroszyński, M. 1991, *MNRAS*, 249, 430
 Jaroszyński, M. 1992, *MNRAS*, 255, 655
 Jaroszyński, M., Park, C., Paczyński, B., & Gott, J. R. 1990, *ApJ*, 365, 22
 Jain, B., Seljak, U., & White, S. 2000, *ApJ*, 530, 547
 Keeton, C. R., & Kochanek, C. S. 1997, *ApJ*, 487, 42
 Kochanek, C. S. 1992, *ApJ*, 384, 1
 Kochanek, C. S. 1996a, *ApJ*, 466, 638
 Kochanek, C. S. 1996b, *ApJ*, 473, 595
 Kochanek, C. S., & Apostolakis, J. 1988, *MNRAS*, 235, 1073
 Kochanek, C. S., & Blandford, R. D. 1987, *ApJ*, 321, 676
 Kochanek, C. S., Falco, E. E., Impey, C., Lehar, J., McLeod, B., & Rix, H.-W. 1998, *CASTLE Survey*,
<http://cfa-www.harvard.edu/castles>
 Krauss, L. M., & White, M. 1992, *ApJ*, 394, 385
 Kundić et al. 1997, *ApJ*, 482, 75
 Linde, A. D. 1982, *Phys.Lett B.*, 108, 289
 Linde, A. D. 1995, *Phys.Lett B.*, 351, 99
 Linde, A. D., & Mezhlumian, A. 1995, *Phys.Rev.D*, 52, 6789
 Maoz, D., & Rix, H.-W. 1993, *ApJ*, 416, 425
 Makino, N., & Tomita, K. 1995, *PASJ*, 47, 117

- Marri, S., & Ferrara, A. 1998, ApJ, 509, 43
- Martel, H. 1995, ApJ, 445, 537
- Martel, H., & Matzner, R. 2000, ApJ, 530, 525
- Martel, H., Premadi, P., & Matzner, R. 1998, ApJ, 497, 512
- Martel, H., Premadi, P., & Matzner, R. 2000, ApJ, 537, 28
- Martel, H., Premadi, P., & Matzner, R. 2001, in preparation
- Martínez-González, E., Sanz, J. S., & Cayón, L. 1997, ApJ, 484, 1
- Munshi, D., & Coles, P. 2000, preprint (astro-ph/0003354)
- Paczynski, B., & Wambsganss, J. 1989, ApJ, 337, 581
- Park, M.-G., & Gott, J. R. 1997, ApJ, 489, 476
- Postman, M., & Geller, M. J. 1984, ApJ, 281, 95
- Premadi, P., Martel, H., & Matzner, R. 1998, ApJ, 493, 10 (Paper I)
- Ratra, B., & Peebles, P. J. E. 1994, ApJ, 432, L5
- Roos, M. & Harun-or-Rashid, S. M. 2000, preprint (astro-ph/0003040)
- Schneider, P., Ehlers, L., & Falco, E. E. 1992, Gravitational Lenses (Berlin: Springer-Verlag) (SEF)
- Schneider, P., & Weiss, A. 1988a, ApJ, 327, 526
- Schneider, P., & Weiss, A. 1988b, ApJ, 330, 1
- Steigman, G., Hata, N., & Felten, J. E. 1999, ApJ, 510, 564
- Turner, E. L. 1990, ApJ, 365, L43
- Turner, M. S.. 1999, In The Third Stromlo Symposium: The Galactic Halo, eds. Gibson, B. K., Axelrod, T. S. & Putman, M. E., ASP Conference Series Vol. 165, 431
- van Waerbeke, L., Bernardeau, F., & Mellier, Y. 1999, A&A, 342, 15
- van Waerbeke, L., et al. 2000, A&A, submitted (astro-ph/0002500)
- Wambsganss, J., Cen, R., & Ostriker, J. P. 1998, ApJ, 494, 29
- Wambsganss, J., Cen, R., Xu, G., & Ostriker, J. P. 1997, ApJ, 475, L81
- Wang, L., Caldwell, R. R., Ostriker, J. P., & Steinhardt, P. J. 2000, ApJ, 530, 17
- Watanabe, K., Sasaki, M., & Tomita, K. 1992, ApJ, 394, 38
- Weinberg, S. 1972, Gravitation and Cosmology (New York: Wiley)
- Weinberg, S. 1989, Rev.Mod.Phys., 61, 1
- White, S. D. M., Frenk, C. S., Davis, M., & Efstathiou, G. 1987, ApJ, 313, 505
- Williams, R. et al. 1996, AJ, 112, 1335
- Williams, R. et al. 1998, in preparation
- Yamamoto, K., Sasaki, M., & Tanaka, T. 1995, ApJ, 455, 412
- Yoshida, H., & Omote, M. 1992, ApJ, 388, L1